Interannual drivers of the seasonal cycle of CO_2 in the Southern Ocean

Luke Gregor[1,2], Schalk Kok[3] and Pedro M. S. Monteiro[1]

[1] Southern Ocean Carbon-Climate Observatory (SOCCO), CSIR, Cape Town, South Africa
[2] University of Cape Town, Department of Oceanography, Cape Town, South Africa
[3] University of Pretoria, Department of Mechanical and Aeronautical Engineering, Pretoria, South Africa

Correspondence to: Luke Gregor (luke.gregor@uct.ac.za)

Abstract. Machine learning has become a useful tool to interpolate ship measurements of pCO_2 (SOCAT) to a gridded map using satellite data. In this study we use an ensemble of three machine learning methods: Support Vector Regression (SVR) and Random Forest Regression (RFR) from Gregor et al. (2017); and the SOM-FFN method from Landschützer et al. (2016). The interpolated data were separated into nine regions defined by basin (Indian, Pacific and Atlantic) and biomes (as defined by Fay and McKinley, 2014a). The regional approach showed a meridional gradient and zonal asymmetry in the magnitude of ΔpCO_2 estimates. Importantly, there was a seasonal decoupling of the modes for summer and winter interannual variability. Winter interannual variability had a longer mode of variability compared to summer, which varied on a 4–6 year time scale. To understand this variability of ΔpCO_2, we investigated changes in summer and winter ΔpCO_2 and the drivers thereof. The dominant winter changes are driven by wind stress variability. This is consistent with the temporal and spatial characteristics of the Southern Annular Mode (SAM), which has a decadal mode of variability (Lovenduski et al., 2008; Landschützer et al., 2016). Interannual trends in summer variability of ΔpCO_2 are consistent with chlorophyll-*a* variability where the latter had high mean seasonal concentrations. In regions of low chlorophyll-*a* concentrations, wind stress and sea surface temperature emerged as stronger drivers of ΔpCO_2. In summary we propose that sub-decadal variability is explained by summer drivers, while winter variability contributes to the long term changes associated with the SAM.

1 Introduction

The Southern Ocean plays a key role in the uptake of anthropogenic CO_2 (Khatiwala et al., 2013; DeVries et al., 2017). Moreover, it has been shown that the Southern Ocean is sensitive to anthropogenically influenced climate variability, such as the intensification of the westerlies (Le Quéré et al., 2007; Lenton et al., 2009; Swart and Fyfe, 2012; DeVries et al., 2017). Until recently, the research community has not been able to accurately measure the contemporary changes, let alone

understand the drivers, of CO_2 in the Southern Ocean due to a paucity of observations (Bakker et al., 2016). Empirical models provide an interim solution to this challenge until prognostic ocean biogeochemical models are able to represent the Southern Ocean CO_2 seasonal cycle accurately (Lenton et al., 2013; Rödenbeck et al., 2015; Mongwe et al., 2016). The research community agrees on large changes in CO_2 fluxes in the Southern Ocean from a source in the 1990's to a sink in the 2000's; however, there is disagreement in the drivers of the changes in CO_2 uptake (Lovenduski et al., 2008; Landschützer et al., 2015; DeVries et al., 2017). This study aims to understand the drivers of the changing CO_2 sink in the Southern Ocean based on an ensemble of empirical estimates using a seasonal analysis framework.

Empirical methods estimate CO_2 by extrapolating the sparse ship based CO_2 measurements using satellite observable proxies. This approach has allowed for a better understanding of the drivers of CO_2 by providing improved spatial and temporal resolution of the variability. Landschützer et al. (2015) showed, using an artificial neural network (ANN), that there was significant strengthening of Southern Ocean CO_2 uptake during the period 2000-2010. While previous studies suggested that changes in wind strength have led to changes in meridional overturning and thus CO_2 uptake (Lenton and Matear, 2007; Lovenduski et al., 2007; Lenton et al., 2009; DeVries et al., 2017), Landschützer et al. (2015) suggested that atmospheric circulation has become more zonally asymmetric since the mid 2000's, which has led to an oceanic dipole of cooling and warming. The net impact of cooling and warming, together with changes in the DIC/TA (Dissolved Inorganic Carbon/Total Alkalinity), led to an increase in the uptake of CO_2 (Landschützer et al., 2015). During this period, in the Atlantic basin, southward advection reduced upwelled DIC in surface waters overcoming the effect of the concomitant warming in the region. Conversely, in the Eastern Pacific sector of the Southern Ocean, strong cooling overwhelmed increased upwelling (Landschützer et al., 2015). Munro et al. (2015) supported this mechanism, with data from the Drake Passage showing that ΔpCO_2 decreased between 2002 and 2014.

In a subsequent study Landschützer et al. (2016) proposed that interannual variability of CO_2 in the Southern Ocean is tied to the decadal variability of the Southern Annular Mode (SAM) – the dominant mode of atmospheric variability in the Southern Hemisphere (Marshall, 2003). This concurs with previous studies, which suggested that the increase in the SAM during the 1990's resulted in the weakening of the Southern Ocean sink (Le Quéré et al., 2007; Lenton and Matear, 2007; Lovenduski et al., 2007; Lenton et al., 2009). The work by Fogt et al. (2012) bridges the gap between the proposed asymmetric atmospheric circulation of Landschützer et al. (2015) and the observed correlation with the SAM of Landschützer et al. (2016). Fogt et al. (2012) show that changes in the SAM have been zonally asymmetric and that this variability is highly seasonal, thus amplifying or suppressing the amplitude of the seasonal mode.

Assessing the changes through a seasonal framework may thus help shed light on the drivers of CO_2 in the Southern Ocean. Southern Ocean seasonal dynamics suggest that the processes driving ΔpCO_2 are complex but with two clear contrasting extremes. In winter, the dominant deep mixing and entrainment processes are zonally uniform driving an increase in ΔpCO_2 with the region south of the Polar Front (PF) becoming a net source and weakening the net sink north of the PF (Lenton et al., 2013). In summer, the picture is more spatially heterogeneous, with net primary production being the primary driver of variability (Mahadevan et al., 2011; Thomalla et al., 2011; Lenton et al., 2013). The competition between light and iron limitation results in heterogeneous distribution of Chl-*a* in both space and time, with similar implications for ΔpCO_2 (Thomalla et al., 2011; Carranza and Gille, 2015). The interaction between the large-scale drivers, such as wind stress, surface heating and mesoscale ocean dynamics, is the primary cause of this complex picture (McGillicuddy, 2016; Mahadevan et al., 2012). Some regions of elevated mesoscale and submesoscale dynamics, mainly in the Sub-Antarctic Zone (SAZ) are also characterized by strong intraseasonal modes in summer primary production and pCO_2 (Thomalla et al., 2011; Monteiro et al., 2015). In general, the opposing effects of mixing and primary production result in the seasonal cycle being the dominant mode of variability in the Southern Ocean (Lenton et al., 2013).

In this study we examine winter and summer interannual variability of ΔpCO_2 from 1998 to 2014 in the Southern Ocean to understand the drivers of long term changes in CO_2 uptake.

2 Empirical methods and data

2.1 Empirical methods and data

In this study we use three machine learning methods: Random Forest Regression (RFR), Support Vector Regression (SVR) and Self-Organising-Maps Feed-Forward Neural Network (SOM-FFN). RFR and SVR are introduced in Gregor et al. (2017) and SOM-FFN is presented in Landschützer et al. (2014). In brief, the RFR approach is an ensemble of decision trees that provides non-linear regression by combining many high variance – low bias estimators (Gregor et al., 2017). SVRs are in principle similar to a single hidden layer FFN, with the difference that SVR statistically determines the complexity of the problem, which is analogous to the hidden layer structure that is typically determined heuristically. The SOM-FFN method is a two-step neural network approach that first clusters data (SOM) and then applies a regression model (FFN) to each cluster.

The SVR and RFR implementations used in this study are trained with the monthly by 1° gridded SOCAT v3 dataset (Bakker et al., 2016). The SOM-FFN (v2.2) used in this study was trained with SOCAT v4 (Landschützer et al., 2017).

Table 1: Three empirical methods used in the ensemble. RFR and SVR are described in Gregor et al. (2017). SOM-FFN is from Landschützer et al. (2016). SST = sea surface temperature, MLD = mixed layer depth, SSS = sea surface salinity, ADT = absolute dynamic topography, Chl-*a* = Chlorophyll-*a*, $pCO_{2(atm)}$ = fugacity of atmospheric CO_2, $xCO_{2(atm)}$ = mole fraction of atmospheric CO_2, Φ(lat, lon) = *N*-vector transformations of latitude and longitude, *t*(day of year) = trigonometric transformation of the day of the year. Note that SOM-FFN uses the de Boyer Montégut et al. (2004) climatology for MLD (dBM2004). The root mean squared errors (RMSE) listed in the last column are for the Southern Ocean from Gregor et al. (2017).

Method	Input variables	RMSE (μatm)
RFR	SST, MLD, SSS, ADT, $Chl\text{-}a_{(clim)}$, $pCO_{2(atm)}$, Φ(lat, lon), *t*(day of year)	16.45
SVR	SST, MLD, SSS, ADT, $Chl\text{-}a_{(clim)}$, $pCO_{2(atm)}$, Φ(lat, lon), *t*(day of year)	24.04
SOM-FFN	SST, $MLD_{dBM2004}$, SSS, Chl-*a*, $xCO_{2(atm)}$	14.84

Table 1 shows the proxy variables used for each of the methods. Sea surface salinity (SSS) and mixed layer depth (MLD) for SVR and RFR are from Estimating the Circulation and Climate of the Ocean, Phase II ($ECCO_2$) (Menemenlis et al., 2008). The use of these assimilative modelled products may in some cases produce results that are unrealistic. This may have influenced the use of the de Boyer Montégut et al. (2004) MLD climatology in the SOM-FFN, where $ECCO_2$ was used in previous iterations of the product. The trade-off of using the climatology is that no changes in MLD are taken into account. We acknowledge that using different proxy variables could result in different ΔpCO_2 estimates, but comparing the different products is beyond the scope of this study. Other data sources that are consistent between methods are: sea surface temperature (SST) and sea-ice fraction by Reynolds et al. (2007), Chlorophyll-*a* (Chl-*a*) by Maritorena and Siegel (2005), absolute dynamic topography (ADT) by Duacs, xCO_2 (CDIAC, 2016) with $pCO_{2(atm)}$ calculated from interpolated xCO_2 using NCEP2 sea level pressure (Kanamitsu et al., 2002). In the case of Chl-*a* for SVR and RFR, Gregor et al. (2017) filled the cloud gaps with climatological Chl-*a*. Note that ADT coverage is limited to regions of no to very low concentrations of sea-ice cover, thus estimates for SVR and RFR methods do not extend into the ice covered regions during winter. Our analyses are thus limited to the regions without ice cover.

Seasonality of the data is preserved by transforming the day of the year (*j*) and is included in both SVR and RFR analyses:

$$t = \begin{pmatrix} \cos\left(j \cdot \frac{2\pi}{365}\right) \\ \sin\left(j \cdot \frac{2\pi}{365}\right) \end{pmatrix} \quad (1)$$

Transformed coordinate vectors are passed to SVR only using *n*-vector transformations of latitude (λ) and longitude (μ) (Gade, 2010; Sasse et al., 2013), with *n* containing:

$$N = \begin{pmatrix} \sin(\lambda) \\ \sin(\mu) \cdot \cos(\lambda) \\ -\cos(\mu) \cdot \sin(\lambda) \end{pmatrix} \quad (2)$$

Wind speed, while not used in the empirical methods, is used in the assessment of the drivers of CO_2. We use CCMP v2, which is an observation-based product that combines remote sensing, ship and weather buoy data (Atlas et al., 2011). Swart et al. (2015a) compared a number of wind reanalysis products with CCMP v1 (where CCMP was the benchmark). The authors found that many of the reanalysis products had spurious trends, particularly in the Southern Hemisphere where data is sparse. Our choice of CCMP, which is based on observations, is thus one that aims to minimise the assumptions that are otherwise made by reanalysis products.

2.2 Uncertainties

The machine learning approaches used in this study are by no means able to estimate ΔpCO_2 with absolute certainty. To account for the uncertainty we use the same approach as Landschützer et al. (2014) to calculate total errors for each of the methods:

$$\boldsymbol{e}_{(t)} = \sqrt{e_{meas}^2 + e_{grid}^2 + e_{map}^2} \quad (3)$$

where $e_{m(t)}$ is the total error associated with a method (m); e_{meas} is the error associated with SOCAT measurements, which is fixed at 5 µatm (Pfeil et al., 2013); e_{grid} is the 5 µatm error associated with gridding the data into monthly by 1° bins (Sabine et al., 2013). Lastly e_{map} is the root mean squared error (RMSE) calculated for each method as shown in Table 1 taken from Gregor et al. (2017).

These errors are used to calculate the average "within-method" error as defined by Gurney et al. (2004):

$$\mathrm{E}_w = \sqrt{\frac{1}{M} \cdot \sum_{m=1}^{M} (e_{m(t)})^2} \quad (4)$$

where $e_{m(t)}$ is the method specific error as defined in Equation 1 and M is the number of methods (3 in this case). For a measure of the difference between methods we use the "between-method" approach used in Gurney et al. (2004):

$$E_b = \sqrt{\frac{1}{M} \sum_{m=1}^{M} (S_m - \bar{S})^2} \quad (5)$$

where S_m is the method estimate of ΔpCO_2 and $\bar{S}$ is the mean of the methods. This is analogous to the standard deviation (for a known population size). We later use an adaptation of this metric as a threshold to determine the confidence around anomalies.

2.3 Regional Coherence Framework

Southern Ocean CO_2 is spatially heterogeneous both zonally and meridionally (Jones et al. 2012). In order to understand this heterogeneity we used the three southernmost biomes defined by Fay and

McKinley (2014a) as done in Rödenbeck et al. (2015). From north to south these are: subtropical seasonally stratified (STSS), sub-polar seasonally stratified (SPSS), seasonally ice covered region (ICE). These three biomes are comparable to the SAZ (Sub-Antarctic Zone), PFZ (Polar-Frontal Zone) and MIZ (Marginal Ice Zone) respectively and will be used throughout the rest of the study. The Southern Ocean is further split into basins where the boundaries are defined by lines of longitude (70°W : Atlantic : 20°E : Indian : 145°E : Pacific : 70°W). Figure 1 depicts these nine regions.

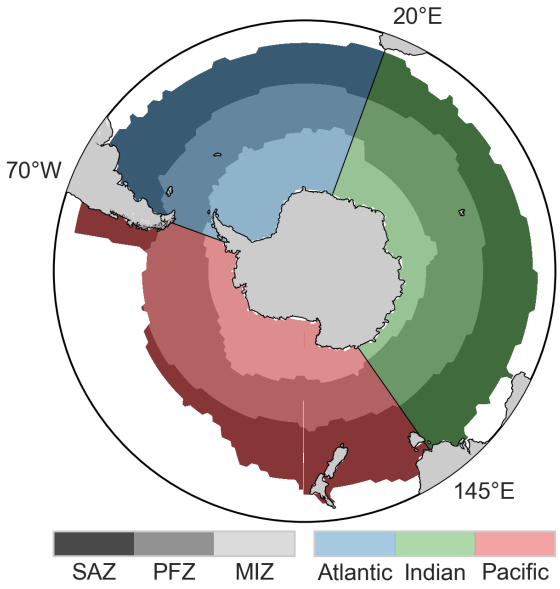

Figure 1: A map showing the regions used throughout this study. The three biomes, SAZ, PFZ and MIZ used in this study are defined by Fay and McKinley (2014a). The regions are also split by basin.

3 Results and discussion

Here we present and discuss the results. The first section examines the uncertainties of the ensemble and its members. We then consider the seasonal cycle of the ensemble mean in time and space. This is done to lay the foundation for the interpretation of the results when assessed with the regional framework. In the regional interpretation the data is decomposed into the nine regions shown in Figure 1. Lastly we implement a seasonal decomposition of the estimates to interpret the drivers of the changes observed in ΔpCO_2.

3.1 Ensemble member performance and variability

Table 2: A regional summary of the errors for the different models. Note that the propagated errors are calculated as shown in equation (3) where the measurement and gridding errors are assumed to be constant at 5 µatm each (Pfeil et al., 2013; Sabine et al., 2013). The within-model and between model errors are calculated using equations (4) and (5) respectively.

Biome	Propagated errors (µatm)			Within model (µatm)	Between model (µatm)
	SVR	RFR	SOM-FFN		
SAZ	17.48	14.50	12.30	14.91	4.88
PFZ	15.94	12.71	13.09	13.99	4.78
MIZ	36.38	24.53	22.46	28.46	10.81
Southern Ocean	**25.06**	**17.91**	**16.44**	**20.16**	**6.79**

We use the RMSE scores as presented in Gregor et al. (2017) with abbreviated results shown in Table 1. The SOM-FFN method has the best score (14.84 µatm). SVR scores the lowest (24.04 µatm), but was still included due to the method's sensitivity to sparse data, which is favourable to the poorly sampled winter period (Gregor et al. 2017). This compliments the RFR method, which scores well (16.45 µatm), but is prone to being insensitive to sparse data (Gregor et al. 2017). These RMSE scores are used to calculate the total errors for each method and region using equation (3) where the measurement and mapping errors are both 5 µatm each (Pfeil et al., 2013; Sabine et al., 2013). These results are shown in Table 2.

Total errors are used to calculate the within-method error, which is an estimate of the combined total errors of the three machine learning methods (equation 4). The between-method errors are the mean of the standard deviation between the methods (equation 5). The within-method errors are much larger than the between-method errors (Table 2). However, the within-method errors are normally distributed and are mechanistically consistent (Gregor et al., 2017). This allows us to observe changes that are smaller than the within-method error. The between-method error (shown in Figure 2d) serves as a better measure of whether observed variability is more than statistical noise as it incorporates the three methodologically different approaches.

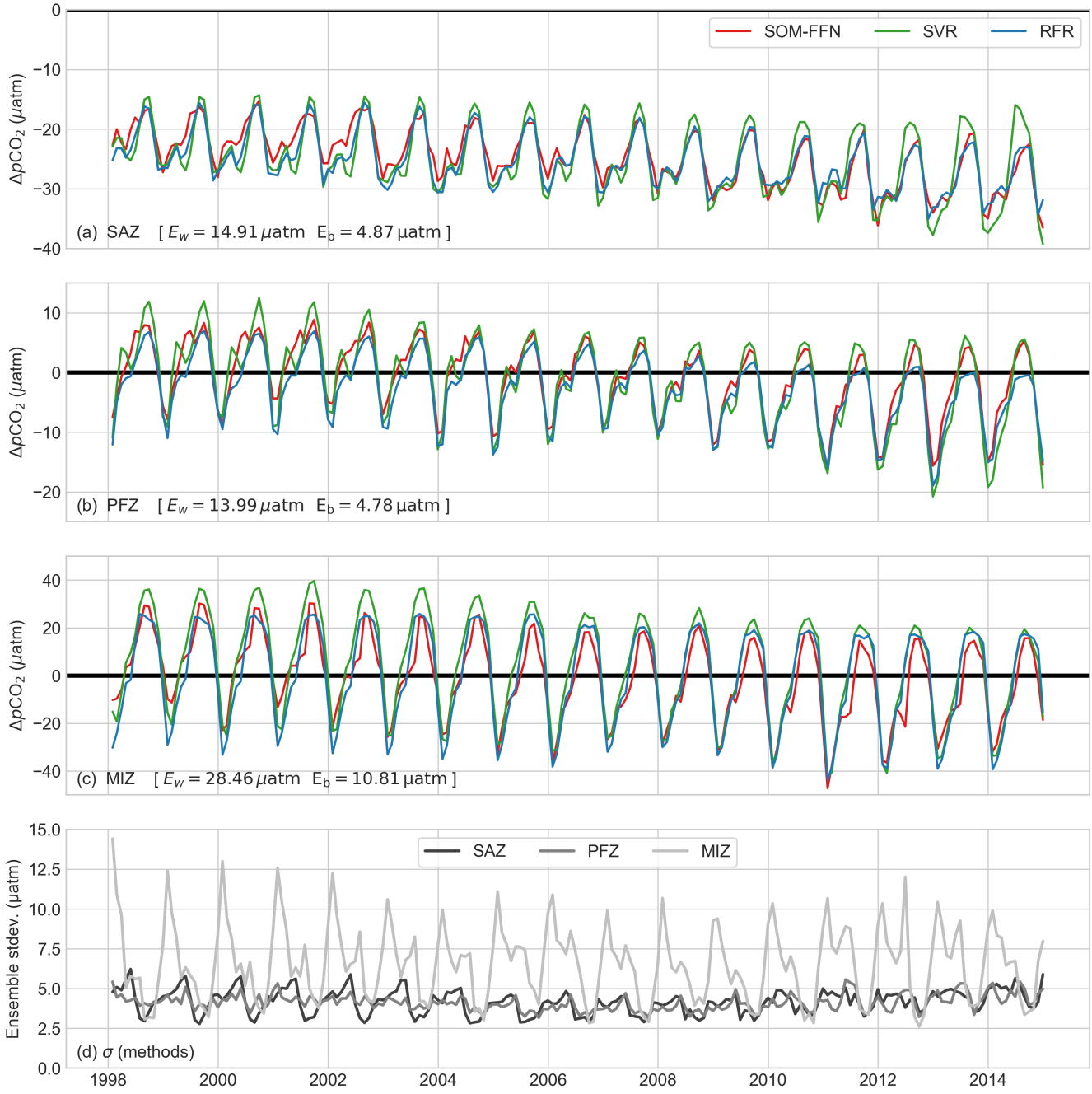

Figure 2: Time series of the three ensemble members for each biome as defined by Fay and McKinley (2014a): (a) SAZ, (b) PFZ, (c) MIZ. (d) shows the standard deviation between ensemble members for the three biomes which is analogous to the between-model error (equation 5). The within-method (E_w) and between-method (E_b) errors are shown for each biome. For a more detailed breakdown of the errors see Table 2.

Figure 2 shows the ΔpCO_2 time series for each of the methods for the three Southern Ocean biomes. The methodological and data driven differences between each of the methods have been addressed in Gregor et al. (2017). In general, there is good agreement amongst the methods with a few notable exceptions. In the SAZ (Figure 2a) the SOM-FFN differs from the other methods for summer and autumn from 1998 to 2008. Gregor et al. (2017) attributed this difference to the clustering step in the SOM-FFN that creates discrepancies in the Atlantic sector. The SVR method overestimates the seasonal amplitude ΔpCO_2 (where the seasonal amplitude is the difference between the winter maxima and summer minima of ΔpCO_2) relative to the other methods for 2012 to 2014. In the PFZ (Figure 2b), the

SVR overestimates ΔpCO_2 relative to the other methods during winter from 1998 to 2004, likely due to the sensitivity to sparse winter data. These differences contribute to the between-method error.

The seasonal amplitude of ΔpCO_2 in the MIZ is much larger than the two other regions. However, this amplitude is likely to be dampened by ice cover (Ishii et al., 1998; Bakker et al., 2008; Butterworth and Miller, 2016). Note that in this study, we do not include regions with sea-ice cover to ensure consistency between methods. Calculated fluxes for this methodologically reduced region will thus under-represent the fluxes of the full extent of the MIZ. We thus exclude the MIZ for the remainder of the study.

Figure 2d shows the time evolution of between-method errors for each biome. This panel highlights the seasonality of the data, specifically the increased heterogeneity of ΔpCO_2 in summer and the impact that this has on ΔpCO_2 estimates. This is due to the more complex competing processes affecting ΔpCO_2 during summer. To gain a better understanding of the seasonal processes we look at the mean state of each season to characterise the drivers of opposing fluxes.

3.2 Ensemble seasonal cycle

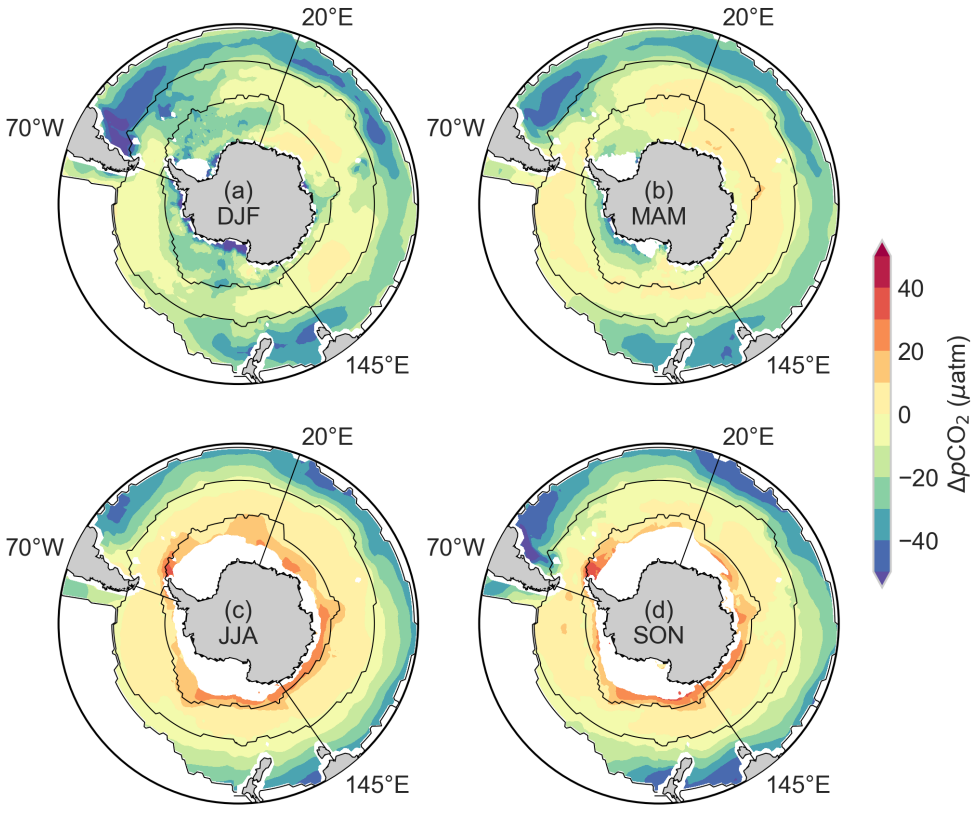

Figure 3: The mean seasonal states of ΔpCO_2 of the empirical ensemble mean. These are shown for (a) summer, (b) autumn, (c) winter and (d) spring. The black contour lines show the SAZ, PFZ and MIZ from north to south as defined by Fay and McKinley (2014a).

The seasonal cycle of the ΔpCO_2 for each biome (Figure 2a-c and Figure 3a-c) is coherent with seasonal processes reported in the literature (Metzl et al., 2006; Thomalla et al., 2011; Lenton et al., 2012;

Lenton et al., 2013). In all biomes, uptake of CO_2 is stronger during summer than in winter giving rise to the strong seasonal cycle. This is due to the opposing influences of the dominant winter and summer drivers, partially damped by the seasonal cycle of temperature (Takahashi et al., 2002; Thomalla et al., 2011; Lenton et al., 2013). The dominant processes of mixing and entrainment in winter result in increased surface pCO_2 and thus outgassing (Takahashi et al., 2009; Lenton et al., 2013; Rodgers et al., 2014). In summer, stratification also allows for increased biological production and the consequent uptake of CO_2, thus reducing the entrained winter DIC and associated pCO_2 (Bakker et al., 2008; Thomalla et al., 2011). However, stratification typically limits entrainment, but does not exclude the occurrence of entrainment during periods of intense mixing driven by storms. This has an impact on primary productivity, DIC and pCO_2 (Lévy et al., 2012; Monteiro et al., 2015; Nicholson et al., 2016; Whitt et al., 2017).

The SAZ (Figure 2a) is a continuous sink where summer uptake (Figure 3a) is enhanced by biological production and winter (Figure 3c) mixing results in a weaker sink (Metzl et al., 2006; Lenton et al., 2012; Lenton et al., 2013). The same processes produce a similar seasonal amplitude in the PFZ (Figure 2b), but stronger upwelling and weaker biological uptake result in a positive shift of the mean. This results in an opposing net summer sink and winter source. However, this is according to the mean state in the PFZ and winter estimates of ΔpCO_2 do in fact approach 0 µatm toward the end of the time series (Figure 2b). The MIZ has the strongest seasonal cycle due to upwelling of CO_2 during winter and strong biological uptake in summer. However, much of this is dampened by sea ice cover during winter and weaker winds during summer (Ishii et al., 1998; Bakker et al., 2008).

Apparent also from Figure 3 is that, over and above the latitudinal gradient, ΔpCO_2 is zonally asymmetric within each biome during summer (Figure 3a), when biological uptake of CO_2 increases. Zonal integration of ΔpCO_2 could thus dampen magnitudes of regional ΔpCO_2. A regional approach is therefore needed to examine the regional characteristics of seasonal and interannual variability of ΔpCO_2 and to understand its drivers.

3.3 Regional ΔpCO_2 variability: zonal and basin contrasts

Here ΔpCO_2 is decomposed into nine domains by biome and basin with the boundaries shown in Figure 1, but note only six are shown in Figure 4. The data are plotted as time series for pCO_2 (Figure 4) showing: mean annual pCO_2 (black lines), the maximum winter values (red line) and the projected summer minima (dashed red line). The projected summer minima (dashed lines) are calculated by subtracting the mean seasonal amplitude from the winter maxima (Figure 4, with air-sea CO_2 fluxes shown in Figure S3). The projected summer minima are the expected summer ΔpCO_2 under the assumption that summer ΔpCO_2 is dependent on, but not restricted to, the baseline set by winter.

Differences between the summer minima and projected minima are highlighted with green and blue patches, highlighting periods of decoupling between summer and winter interannual variability. The green areas indicate periods of strong uptake (relative to winter) that enhance the mean uptake of CO_2 and amplify the seasonal cycle. Conversely, blue areas show periods where weak summer uptake (relative to winter) offsets winter outgassing, thus reducing the mean ΔpCO_2 as well as supressing the amplitude of the seasonal cycle (Figure 4).

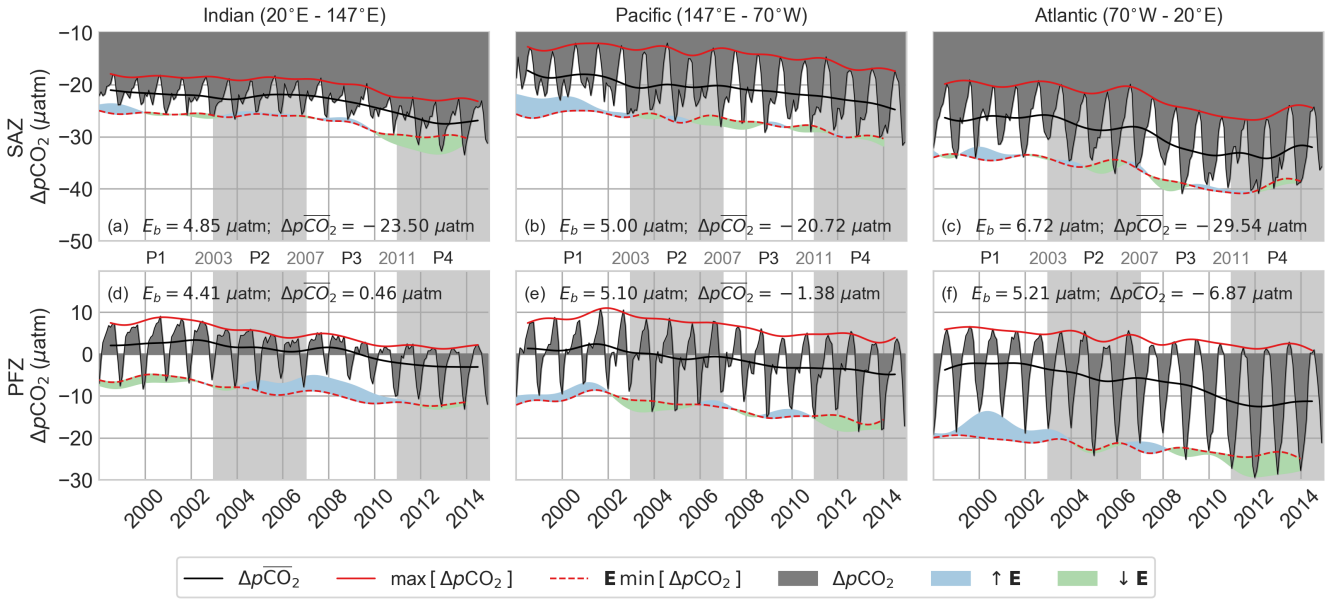

Figure 4: Figures (a-f) show the ensemble mean of ΔpCO_2 (dark grey) plotted by biome (rows) and basin (columns). Biomes are defined by Fay and McKinley (2014a). The solid red line shows the maximum for each year (winter outgassing) and the dashed line shows the same line less the average seasonal amplitude – this is the expected amplitude. The shaded blue (green) area shows when the annual minimum is less (greater) than the expected amplitude. E_b is the average between-method error and $\Delta p\overline{CO}_2$ is the average for the entire time series. Light grey shading in (a-f) shows the periods used in Figure 5 and Figure 6.

The data for ΔpCO_2 (Figure 4) show that the Southern Ocean sink strengthened from 2002 to 2011 in all domains, a period identified as the *reinvigoration* by Landschützer et al. (2015). This was preceded by a period of a net weakening sink in the 1990's referred to as the *saturation* period after Le Quéré et al. (2007). In the period from 2012 to 2014, three domains (Figure 4a,c,f) go from growing uptake to reducing uptake; however, our confidence in the changing trend is low due to lack of coherence between methods (Figure 2a,b) and only three years of data, with little data in 2014.

A key feature of Figure 4 is that the mean interannual variability is the net effect of decoupled seasonal modes of variability for summer and winter. This is particularly evident in the PFZ (Figures 4d-f). Here, and in the other biomes, the net strengthening of the CO_2 sink is mainly linked to a reduction of ΔpCO_2 in winter for the majority of the time series. This corresponds with the findings of Landschützer et al. (2016), who linked the reinvigoration to the decadal variability of the Southern Annular Mode (SAM) – the dominant mode of atmospheric variability in the Southern Hemisphere (Marshall, 2003). In contrast, summer ΔpCO_2 variability is shorter (roughly 4 – 6 years), thus providing inter-annual modulation of longer time-scale winter variability. This is demonstrated well in the Indian sector of the PFZ where a

decrease in winter ΔpCO_2 from 2002 to 2011 is offset by weakening of the summer sink from 2006 to 2010 (Figure 4d). Similarly in the Atlantic and Pacific sectors of the PFZ decoupling occurs from ~2011 to the end of 2014 with a rapid increase in the strength of the summer sink.

The mean amplitude of the seasonal cycle of ΔpCO_2, the mean difference between the summer minima and the winter maxima, is a better means of understanding the strength of the seasonal drivers than the mean ΔpCO_2. For example the Atlantic sectors of the SAZ and PFZ (Figures 4c,f) have the strongest seasonal variability (14.11 and 25.83 µatm respectively). This contrasts the relatively weak seasonal amplitude in the Indian sector of the Southern Ocean which has mean amplitudes of 7.06 and 13.64 µatm for the SAZ and PFZ respectively (Figures 4b,e). This contrast can also be seen by comparing the mean seasonal maps of ΔpCO_2 in Figures 3a and 3c. In summer, strong uptake in the eastern Atlantic sector of the Southern Ocean is indicative of large biological drawdown of CO_2 by phytoplankton (Thomalla et al., 2011). Conversely, relatively low primary production in the Indian sectors of the SAZ and PFZ results in a small seasonal amplitude (Thomalla et al., 2011). This large discrepancy in biological primary production is related to the availability of iron, a micronutrient required for photosynthesis. The lack of large land masses, a source of iron, in the Indian sector of the Southern Ocean could be a contributing factor to the lack of biomass (Boyd and Ellwood, 2010; Thomalla et al., 2011).

3.4 Seasonal deconstruction of interannual variability

Figure 4 gives us insight into the magnitude of interannual ΔpCO_2 variability as well as the character of these changes; *i.e.* decoupling of interannual winter and summer modes of variability. This alludes to the point that ΔpCO_2 is responding to different adjustments of seasonal large scale atmospheric forcing and/or responses of internal ocean dynamics in the Southern Ocean (Landschützer et al., 2015, 2016; DeVries et al., 2017).

In order to capture the decoupled short term variability observed during summer, the data are divided into four interannual periods (P1 to P4), where P1 is five years and the remaining periods (P2 to P4) are four years as shown by the light grey fills in Figure 4. The small discrepancy in the length of the periods is due to the uneven length of the time series (17 years).

These four periods are too short for trend analyses (Fay and McKinley, 2014b), but the intention here is to identify periods that are short enough to resolve interannual changes of large-scale drivers of the winter and summer pCO_2 that would otherwise be averaged out over longer periods. We then calculate the relative anomaly between each successive period rather than an anomaly of the mean state (*e.g.* P2 – P1). As a result four periods give rise to three sub-decadal-scale transition anomalies for summer and

winter: *A* (P2 – P1), *B* (P3 – P2) and *C* (P4 – P3). We do this separately for each method rather than using the ensemble mean (see S4 for calculations). The mean of the method anomalies for each transition is then taken. These anomalies are considered significant if the absolute estimate of the anomaly is larger than the standard deviation between the methods for each period. These calculations along with plots for the standard deviation between methods are shown in the supplementary materials in S4.

Note that, although only summer and winter anomalies are discussed, it is recognised that autumn and spring could be equally mechanistically important. Winter anomalies of ΔpCO_2, wind stress, SST and MLD are shown in Figure 5. Summer anomalies of ΔpCO_2, wind stress, SST and Chl-*a* are shown in Figure 6 where MLD, in winter, is replaced with Chl-*a* for summer as it is potentially a more important driver than the generally shallow summer MLD (the omitted plots are shown in Figures S5 and S6).

3.5 Drivers of winter ΔpCO_2 variability

We will limit the interpretation of the changes to the regions where the anomaly is larger than the between-method error of anomalies (see S4 for calculations and maps). This masks out large regions, but three key points still arise from the significant anomalies. Firstly, ΔpCO_2 is often spatially roughly coherent with wind stress and the inverse of SST. Secondly, there is a dipole in the wind anomalies in the Indian and Pacific between transitions A and B. This is confirmed by the *u*- and *v*-components of wind shown in the supplementary materials (Figure S5). Lastly, the Indian sector of the Southern Ocean dominates the reinvigoration of the CO_2 sink. These points are now addressed in more detail.

Transition A (P2 – P1) shows a relative increase of ΔpCO_2 in the east Indian and Pacific sectors of the SAZ – suggesting a delay in the onset of the reinvigoration for these basins. This regional sustained saturation corresponds to a shift towards stronger winds and/or deeper MLDs in the west Pacific sector of the SAZ (Figure 5d,j). In contrast, CO_2 uptake in the east Atlantic and west Indian sectors of the SAZ start to strengthen, which roughly corresponds with the weaker winds.

Transition B (P3 – P2) is characterized by a further intensification of the invigoration of ΔpCO_2 (negative shift) primarily in the Indian basin (Figure 5b). Once again the strengthening of the CO_2 uptake corresponds with weaker wind stress, a warming trend in surface waters and shoaling MLDs in the eastern Atlantic and Indian Ocean sectors of the SAZ and PFZ (Figure 5b,e,h,k). The opposing effects of the dipole are observed east of New Zealand where stronger wind stress, deeper MLD, and cooler surface waters correspond with a positive shift in ΔpCO_2.

In transition C (P4 – P3), the ΔpCO_2 sink strengthens further in the northern extremes of the east Indian and west Pacific basins. This negative shift corresponds well with strong shoaling of the MLD (Figure 5l). The west Pacific sector of the PFZ shows a positive shift in ΔpCO_2, which is coherent with an increase in the wind stress and deepening MLD.

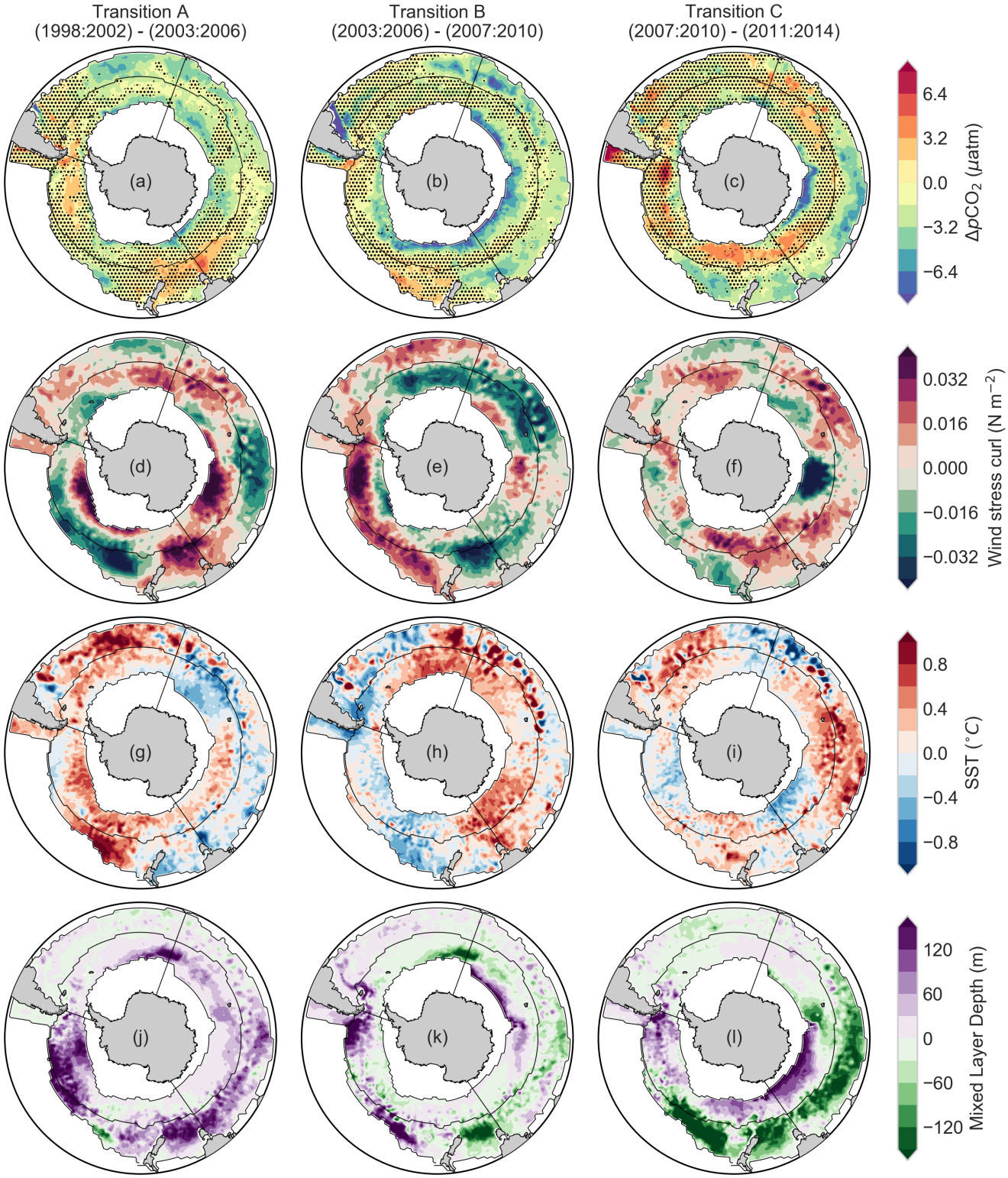

Figure 5:Transitions (relative anomalies) of winter ΔpCO_2 (a-c), wind stress (d-f), sea surface temperature (g-i) and mixed layer depth (j-l) for four periods. The thin black lines show the boundaries for each of the nine regions described by the biomes (Fay and McKinley, 2014a) and basin boundaries. Regions with dots in (a-c) are where the anomalies are not significant ie: standard deviation of the anomalies between models is greater than the absolute mean of method anomalies as described in equations S1 to S3.

3.5.1 Wind dominated interannual variability of pCO_2 in winter

Based on the observations outlined above, we propose that interannual variability of the regional (basin-scale) characteristics of winter wind stress may be the dominant driver of the saturation and reinvigoration periods.

These findings suggest that increasing or decreasing interannual winter wind stress variability impacts ΔpCO_2 (and thus FCO_2) by driving changes in turbulent mixing that set the magnitudes of winter entrainment. In the transition to and during winter, this mixing is associated with changes in rates of heat loss that drive loss of buoyancy or weaker stratification (Abernathey et al., 2011). Weaker buoyancy facilitates deepening of the MLD, thus entraining DIC-rich deep waters (Abernathey et al., 2011; Lenton et al., 2013). Conversely, decreased wind stress and mixing during winter (on seasonal or interannual time scales) reduces the rate of heat loss (represented as warm anomalies in Figure 5). This results in stronger stratification and shallower winter MLD limits entrainment of DIC, which strengthens the CO_2 winter disequilibrium and leads to a stronger CO_2 sink anomaly (Figure 5). These are the mechanisms that we propose result in decreasing or increasing fluxes with interannual and basin–scale changes in wind stress.

We propose the link between spatial changes in wind stress and uptake of CO_2 as an alternative hypothesis to temperature being a driver as suggested by Landschützer et al. (2015). Typically an increase in ocean temperature, which reduces CO_2 solubility, results in an increase in ΔpCO_2 (Takahashi et al., 1993). However, seasonal – regional analysis shows that the observed relationship between pCO_2 and SST is counterintuitive (Figure 5a-c,g-i). On this basis we propose that SST is not a driver of pCO_2 in winter. We suggest that this relationship is a product of weaker mixing and Ekman transport that allows warmer waters to shift southward. This also has the impact of strengthening buoyancy that would otherwise bring CO_2 to the surface. In summary, our results suggest that, like pCO_2, the SST changes are also a response to the wind stress and not in themselves the drivers of pCO_2 changes.

Given the hypothesis that wind stress is the dominant driver of interannual – decadal ΔpCO_2 in winter, it is of interest to understand its potential mechanisms. Past studies have used the SAM as a proxy for wind stress variability over the Southern Ocean, where the multi-decadal increasing trend has been cited as a reason for the saturation in the 1990's (Marshall, 2003; Le Quéré et al., 2007; Lenton and Matear, 2007; Lovenduski et al., 2008). While Landschützer et al. (2016) identified the SAM as being a driver of global CO_2 variability, the index does not explain the reinvigoration of the Southern Ocean CO_2 sink in the 2000s. The SAM is often represented as a zonally integrating index (Marshall, 2003), but more recent studies have shown that the SAM, as the first empirical mode of atmospheric variability, is

zonally asymmetric (Fogt et al., 2012). The zonal asymmetry of the SAM is linked with the El Niño – Southern Oscillation and is strongest in winter, particularly over the Pacific sector of the Southern Ocean during a positive phase, thus in accord with the Pacific–Indian winter wind stress dipole observed in Figures 5d,e (Barnes and Hartmann, 2010; Fogt et al., 2012). Fogt et al. (2012) noted that the SAM has become more zonally symmetric in summer since the 1980's, matching the wind stress anomalies seen in Figure 6d-f.

In summary, we propose that interannual variability of wind stress and its regional expression in winter is the dominant interannual driver of ΔpCO_2 variability in the Southern Ocean. The interannual variability of wind stress is linked to the SAM, but this relationship is nuanced by the zonally (regional) asymmetric variability of the SAM as observed by zonal asymmetry of wind stress in the Pacific and Indian sectors of the Southern Ocean.

3.6 Anomalies of ΔpCO_2 and its summer drivers

The most marked difference between the summer and winter anomalies, is that ΔpCO_2 (Figures 6a-c) does not correlate with wind stress (Figures 6d-f), thus ruling out wind as a first order driver of summer CO_2. Rather, ΔpCO_2 has the strongest coherence with Chl-*a* (an inverse relationship), which suggests that primary production may be a first order driver of the observed ΔpCO_2 variability. Another difference between summer and winter is that the magnitudes of the transition anomalies are much larger in summer, and thus there are larger regions of significant anomalies (Figure 6a-c).

Looking more specifically at the significant variability of ΔpCO_2, transition A (P2 – P1 in Figure 6a) is marked by a decrease of CO_2 in the SAZ (Tasman shelf region), mirrored by an increase in Chl-*a*. The Atlantic and Indian sectors of the PFZ remain mostly neutral/weak sources marked by a reduction in phytoplankton biomass (Figure 6j). Transition B (P3 – P2 in Figure 6b), shows invigoration of CO_2 uptake in the Atlantic sector of the SAZ and PFZ; and in parts of the Pacific Ocean. Once again, the reduction of ΔpCO_2 correlates well with Chl-*a* increases. In transition C (P4 – P3 in Figure 6c) the reduction of the ΔpCO_2 is widespread in the Indian and Pacific Oceans in all three biomes, as the increase in Chl-*a* is similarly widespread. Conversely, there is a reduction in Chl-*a* and concomitant increase in ΔpCO_2 along Polar front in the Atlantic sector, coinciding with position of the ACC, which has high EKE (Meredith, 2016). These examples demonstrate that ΔpCO_2 is driven primarily by Chl-*a* in summer. However, understanding Chl-*a* variability is more complex as there is seemingly no set rule between Chl-*a*, SST and wind stress (Thomalla et al., 2011).

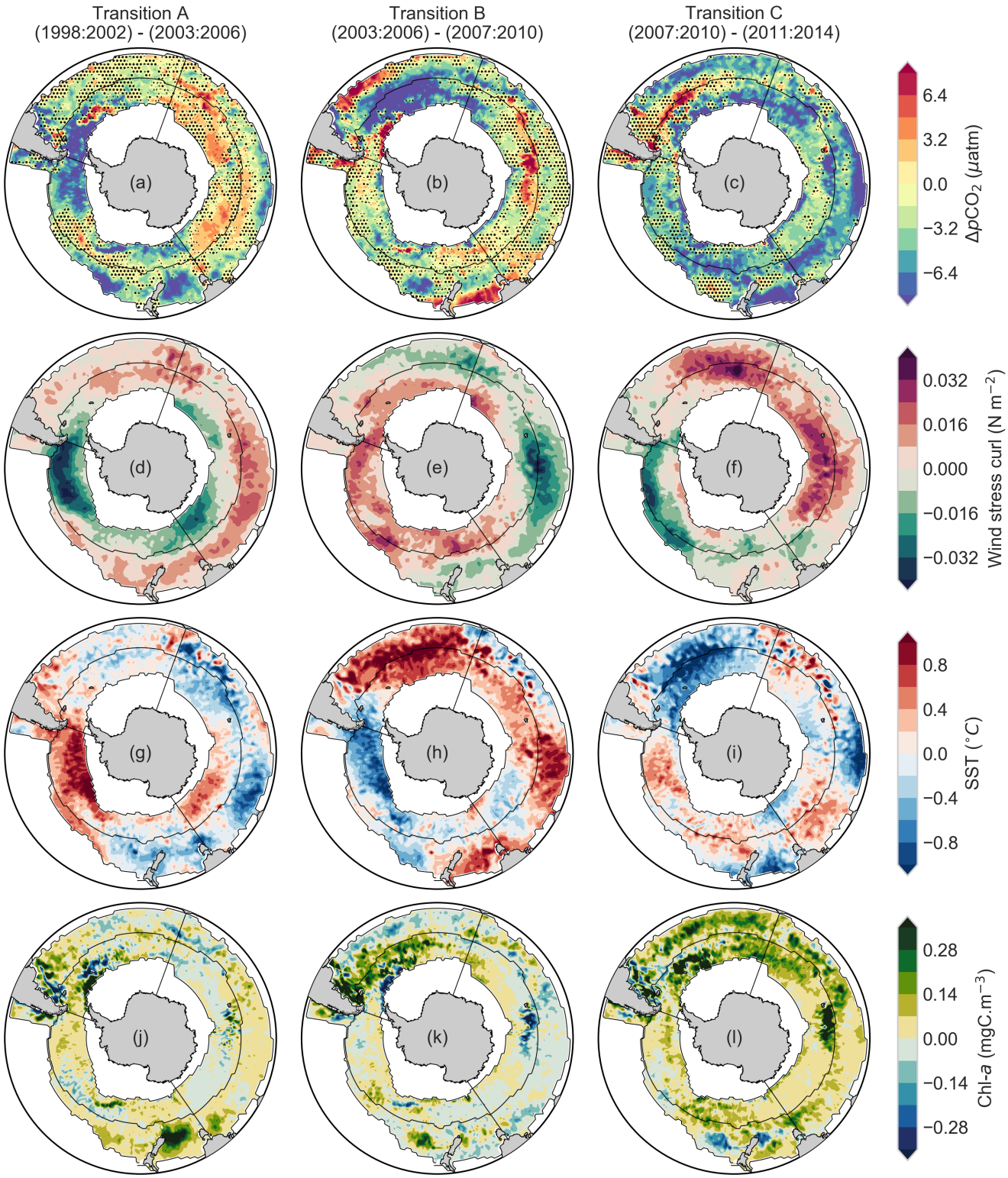

Figure 6: Relative anomalies of summer ΔpCO_2 (a-c), wind stress (d-f), sea surface temperature (g-i) and mixed layer depth (j-l) for four periods (as shown above each column). The thin black lines show the boundaries for each of the nine regions described by the biomes (Fay and McKinley, 2014a) and basin boundaries.

There are regions in the Southern Ocean where summer Chl-*a* variability does not coincide with ΔpCO_2 variability, particularly in the Indian and Pacific sectors of the SAZ (Figures 6a-c and 6j-l). This may be due to low chlorophyll concentrations, and anomalies thereof, in these regions (Thomalla et al., 2011). As a result the other variables, SST and wind stress, may be higher order drivers in low chlorophyll regions, as found by Landschützer et al. (2015) and Munro et al. (2015).

It is thus important to understand the variability of SST and wind stress in summer. Large SST anomalies between the western Atlantic and eastern Pacific sectors vary as a zonally asymmetric dipole. As in winter, there is a summer wind stress anomaly dipole, but rather than being zonally asymmetric (*e.g.* Pacific–Indian), the dipole has annular, north-south variability (Figures 5,6d-f). We suggest that these dipoles in the variability may indicate that the Southern Ocean, as a system, transitions between different states forced by atmospheric variability (Landschützer et al., 2015).

An important note is that the magnitudes of ΔpCO_2 and its drivers have different magnitudes seasonally. For example, the anomalies of ΔpCO_2 and SST are larger in summer than in winter. Conversely, the wind stress anomalies are larger for winter than in summer. This is an important consideration for analyses that aim to understand the driving mechanisms, where annual averaging would make it difficult to decompose the true drivers of change.

3.6.1 Chlorophyll dominated interannual anomalies of pCO_2 in summer

Our finding that Chl-*a* is the dominant driver of interannual ΔpCO_2 variability should not be surprising given that models and observations support this notion (Hoppema et al., 1999; Bakker et al., 2008; Mahadevan et al., 2011; Wang et al., 2012; Hauck et al., 2013; 2015; Shetye et al., 2015). However, our data show that the dominance of interannual Chl-*a* variability over ΔpCO_2 is largely limited to regions where Chl-*a* is high, such as the Atlantic, the Agulhas retroflection and south of Australia and New Zealand (Figure 7).

The spatial variability of high Chl-*a* regions in the Southern Ocean is complex due to the dynamics of light and iron limitation (Arrigo et al., 2008; Boyd and Ellwood, 2010; Thomalla et al., 2011; Tagliabue et al., 2014; 2017). This complexity is highlighted in Thomalla et al. (2011), where the Chl-*a* is characterized into regions of concentration and seasonal cycle reproducibility (Figure 7). The seasonal cycle reproducibility (SCR) is calculated as the correlation between the mean annual seasonal cycle and the observed chlorophyll time series. Here we use the approach of Thomalla et al. (2011), in Figure 7, as a conceptual framework to understand the interannual variability of ΔpCO_2.

3.6.2 High chlorophyll regions

While regions of high SCR (dark green in Figure 7) do not correspond with the interannual variability of Chl-*a* (Figure 6j-l), the framework by Thomalla et al. (2011) does present a hypothesis by which the variability of Chl-*a* and its drivers can be interpreted. This is, that the variability of Chl-*a* in a region is a complex interaction of the response of the underlying physics (mixing vs. buoyancy forcing), which modulate light (via the MLD) and iron supply, to the interannual variability in the drivers (SST and

wind stress). This complexity is exemplified by strong warming in the Atlantic during transition B, which results in both an increase and decrease in Chl-*a*, with inverse consequences for ΔpCO_2. The effect is an even stronger transition C, where strong cooling in the Atlantic results in both a decrease and increase of Chl-*a* (Figure 6i,l). In both transition A and B the respective increase and decrease of Chl-*a* occur roughly over the ACC, while the opposing effects during transitions A and B occur roughly to the north and south of the ACC region. These temperature changes may impact the stratification of the region, but complex interaction with the underlying physics results in variable changes in Chl-*a*.

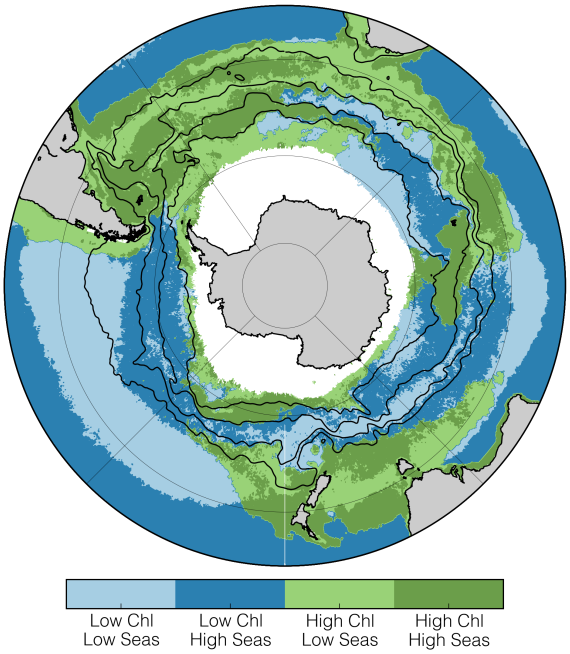

Figure 9: Chl-*a* seasonal cycle reproducibility and iron supply mechanisms in the Southern Ocean (a) Regions of chlorophyll biomass and seasonal cycle reproducibility from Thomalla et al. (2011) (using SeaWIFS data). Seasonality is calculated as the correlation between the mean annual seasonal cycle compared to the observed chlorophyll time series. A correlation threshold of 0.4 was applied to each time series to distinguish between regions of high and low seasonality; similarly, a threshold of 0.25 mg m^{-3} was used to distinguish between low or high chlorophyll waters. Black lines show the Southern Ocean fronts calculated by sea surface height (Swart et al., 2010).

It is clear that, while there is a relationship between Chl-*a* and pCO_2 as well as a relationship between wind stress and SST in summer, the relationship between wind forcing, Chl-*a* and pCO_2 is not as strong as in the winter anomalies (Figure 5). It may be that enhanced summer buoyancy forcing resulting from summer warming and mixed layer eddies drives a more complex response to wind stress in the form of vertical velocities and mixing, which influence the iron supply and the mixing depth (McGillicuddy, 2016; Mahadevan et al., 2012).

Mesoscale and sub-mesoscale processes may have a part to play in these dynamic responses of Chl-*a* to changes in SST and wind stress (amongst other drivers). For example, eddy-driven slumping could act to rapidly shoal the mixed layer (Mahadevan et al., 2012; Swart et al., 2015b; du Plessis et al., 2017). This allows phytoplankton to remain within the euphotic zone and thus grow (while iron is not limiting). Similarly, Nicholson et al. (2016) and Whitt et al. (2017) demonstrated that submesoscale

processes could supply iron to the mixed layer by submesoscale mixing. Importantly, these mechanisms rely on a mixing transition layer that has sufficient iron that is able to sustain growth. Weak dissolved iron gradients in the Pacific and east Indian sectors of the Southern Ocean could explain the lack of phytoplankton in these regions (Tagliabue et al., 2014; Nicholson et al., 2016). Much of the spatial character of the transition anomalies occurs at mesoscale, which strengthens the view that these mesoscale and sub-mesoscale processes may be key to explain changes in Chl-*a* (Figure 6j-l).

3.6.3 Low chlorophyll regions

Entrainment and stratification can explain much of the variability in the eastern Pacific and Indian sector of the PFZ (with the exception of the wake of the Kerguelen Plateau). For example, in the eastern Pacific in transition A (Figure 6a,d,g), strong warming and weaker winds have little impact on Chl-*a*, but a decrease in ΔpCO_2 is observed. Conversely, cooling in the west Indian sector of the PFZ results in a weak increase in ΔpCO_2 during the same transition. In both these cases, the effect of cooling or warming on ΔpCO_2 is negligible relative to the impact of entrainment or stratification respectively. The effect is reversed in the eastern Pacific during transition B where strong cooling results in a weak reduction of ΔpCO_2 rather than the increase that would be expected from entrainment. This is the mechanism that Landschützer et al. (2015) ascribed to the reduction of ΔpCO_2 in the Pacific, but the effect observed in Figure 6b is weak.

In summary, regions with high biomass Chl-*a* integrates the complex interactions between SST, wind stress, MLD and sub-mesoscale variability resulting in large interannual pCO_2 variability compared to low biomass regions. In low Chl-*a* regions, wind driven entrainment/stratification are more likely drivers of ΔpCO_2.

4 Synthesis

In this study, an ensemble mean of empirically estimated ΔpCO_2 is used to investigate the trends and the drivers of these trends in the Southern Ocean. The estimated ΔpCO_2 shows that the seasonal cycle is the dominant mode of variability imposed upon weaker interannual variability. The data are separated into domains defined by functional biomes and oceanic basins to account for the roughly basin scale zonal asymmetry observed in preliminary analyses of ΔpCO_2 (Fay and McKinley, 2014a). A seasonal decomposition is applied to the domains, revealing that winter and summer variability is decoupled for each region. The increase and subsequent decrease of pCO_2 (and air-sea CO_2 fluxes) is in accordance with recent studies showing a saturation of the Southern Ocean CO_2 sink in the 1990's followed by the reinvigoration in the 2000's (Le Quéré et al., 2007; Landschützer et al., 2015).

We suggest that changes in the characteristics of the seasonal cycle of the drivers of pCO_2 define the interannual variability pCO_2. In other words, the mechanisms that drive interannual modes of variability are embedded in the seasonal cycle.

We propose that winter ΔpCO_2 variability is driven primarily by changes in winter wind stress, which influences the resulting convective entrainment of deep DIC-rich water masses (Lenton et al., 2009; 2013). This winter variability has a longer mode than summer inter-annual variability. We attribute this longer winter mode of variability to the Southern Annular Mode, which has a decadal mode (Lovenduski et al., 2008; Fogt et al., 2012; Landschützer et al., 2016). This mechanism is likely dominant in winter due to its role in large seasonal net heat losses that drive convective overturning of the water column.

We suggest that interannual summer variability of ΔpCO_2 occurs from a baseline set by an interannual winter trend. Moreover, the shorter time-scale summer interannual variability of ΔpCO_2 (roughly 4 – 6 years) is driven primarily by Chl-*a*. Wind stress and sea surface temperature still influence ΔpCO_2 in summer, but are lower order drivers. We propose that the interannual variability of the summer seasonal peak is linked to the complex interaction of mid-latitude storms with the strong mesoscale and sub-mesoscale gradients in the Southern Ocean.

Overall, we propose that although the winter wind stress linked mechanisms explain the decadal trends in the strengthening and weakening of CO_2 uptake by the Southern Ocean, summer drivers may explain the inter-annual variability in the decadal trends (Lovenduski et al., 2008; Landschützer et al., 2015).

Lastly the ensemble of machine learning methods shows that there is still considerable disagreement between the different approaches. This is likely driven by the lack of pCO_2 measurements in the Southern Ocean as found by Rödenbeck et al. (2015). Autonomous sampling platforms will likely play a role in closing this “observation gap”, but strategic deployment and sampling strategies will be critical to constrain and improve our understanding of CO_2 in the non-stationary context (McNeil and Matear, 2013; Monteiro et al., 2015).

S Supplementary Materials

S1 Wind speed and regional surface area

The regional magnitude of integrated air-sea CO_2 fluxes is in part determined by the wind speed and surface area of the specific region. Figure S1a shows the average wind speeds for summer and winter for each of the regions as defined in Figure 1. The wind product used is CCMP v2 (Atlas et al. 2011). Figure S1b shows the surface area of each of the regions. Note that the Indian sector of the PFZ has both the highest average wind speed and has the largest surface area. This explains the dominance of the region in the determination of interannual variability of FCO_2 (Figure S2), even though ΔpCO_2 (Figure 4) variability is relatively weak.

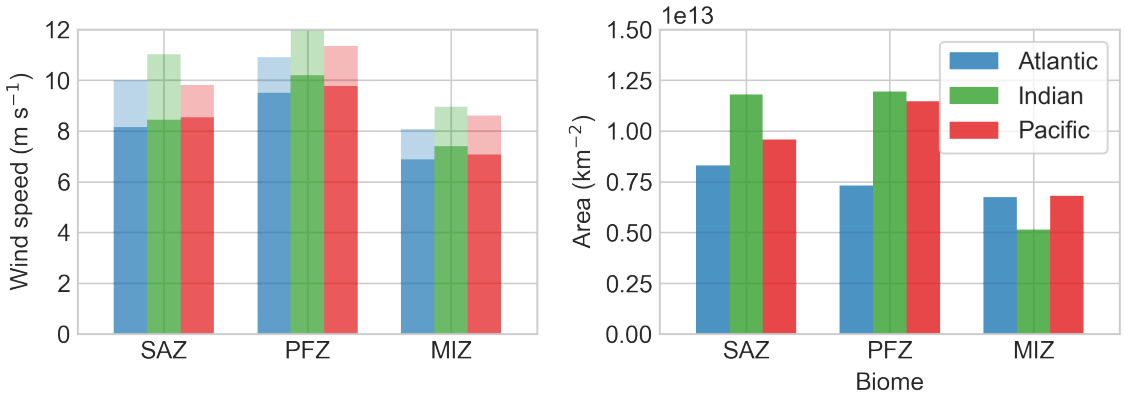

(a) **(b)**

Figure S1: (a) Average wind speeds for each of the biomes for summer (dark) and winter (light). The ocean basins are shown by the colours as shown in the key for (b). (b) shows the size of each region separated by biome and basin.

S2 Seasonal time series

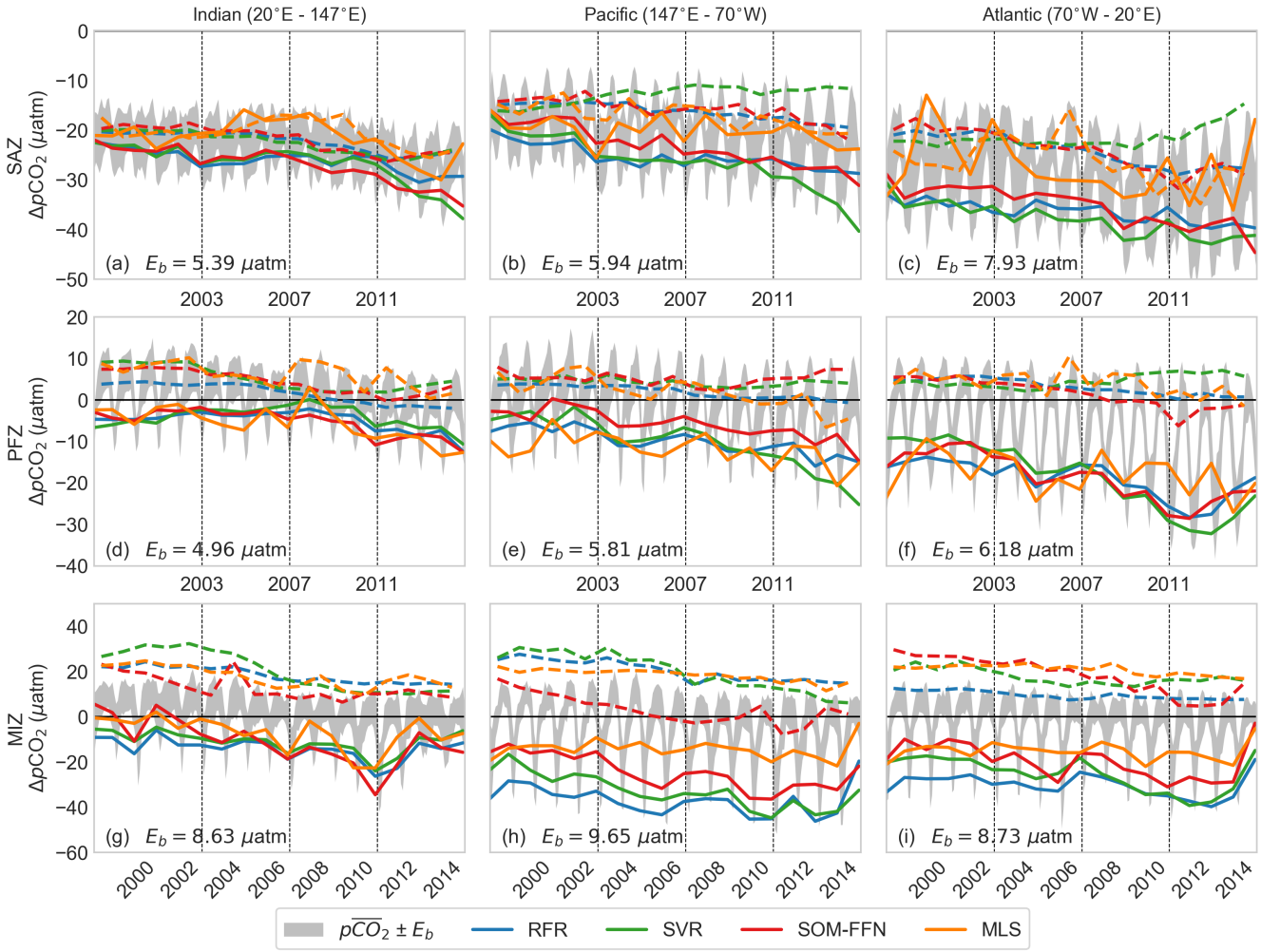

Figure S2: The regional breakdown of the seasonal averages for ΔpCO_2. The seasonal mean for summer (solid) and winter (dashed) for each method is represented by the different coloured lines as shown in the key, where MLS is the Mixed Layer Scheme. The other methods are as in the main text. The grey fill is the ensemble mean $\Delta pCO_2 \pm E_b$ where E_b is the between-method error calculated as in Eq (5).

Figure S2 shows the seasonal time series for each region maintaining separate seasonal averages for each method. We also include the Marginal Ice Zone plots with all plots showing the average between-method error.

The Mixed Layer Scheme (MLS) method by Rödenbeck et al. (2013) is also included. Note that the MLS is not a machine learning method as it incorporates prior knowledge of the system. The method results in divergent estimates of ΔpCO_2, particularly in the SAZ. The MLS fails to produce a seasonal cycle with winter and summer ΔpCO_2 having the same magnitude. Further work will have to be done to understand the cause for this difference. We do not include MLS in the main ensemble as we cannot explain this difference. The methods are in much better agreement in the PFZ and MIZ.

S3 Air-Sea CO_2 Fluxes

Air sea CO_2 fluxes are calculated with:

$$FCO_2 = k_w \cdot K_0 \cdot (pCO_2^{sea} - pCO_2^{atm}) \quad \text{(S1)}$$

The gas transfer velocity (k_w) is calculated using a quadratic dependency of wind speed with the coefficients of (Wanninkhof et al., 2009). Coefficients from Weiss (1974) are used to calculate K_0 and ΔpCO_2 is estimated by the empirical models. Wind speed is calculated from the u and v vectors ($\sqrt{u^2 + v^2}$) of the Cross-Calibrated Multiplatform Product (CCMP) v2 (Atlas et al., 2011; Wentz et al., 2015). Wind speed is one of the largest contributors to the uncertainty in flux estimates, thus the choice of the wind product could have a large impact on flux estimates as well as interpretation of the drivers of CO_2 (Takahashi et al., 2009). We use the ensemble mean ΔpCO_2 from Figure 4 to calculate fluxes - note that this does not include the MLS shown in Figure S2.

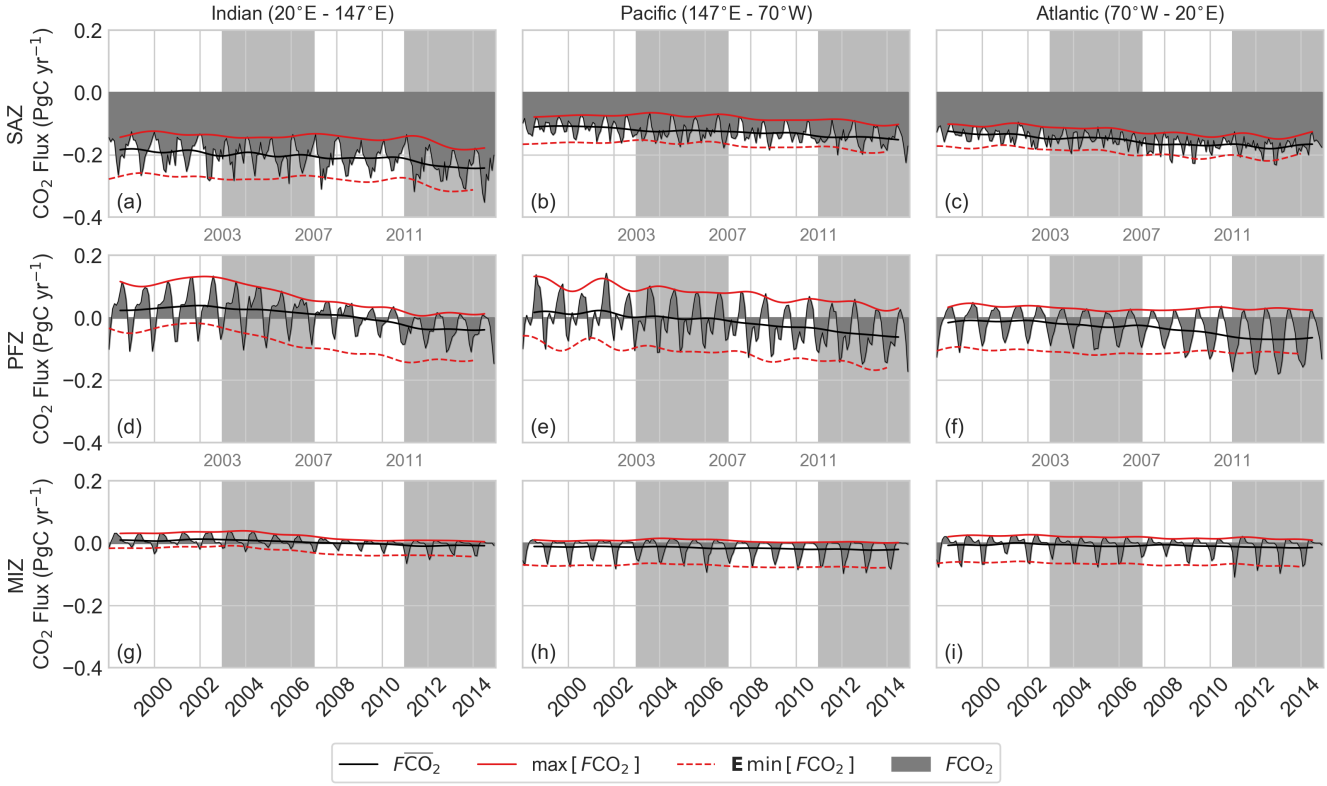

Figure S3: FCO_2 (dark grey) plotted by biome (rows) and basin (columns). Biomes are defined by Fay and McKinley (2014a). The solid red line shows the maximum for each year (winter outgassing) and the dashed line shows the same line less the average difference between the minimum and maximum – this is the expected amplitude. Lighter grey shading in (a-i) shows periods used in Figure 5 and 6. Note that fluxes in the MIZ are calculated from a reduced surface area to maintain consistency between methods.

Mean FCO_2 is shown in Figure S3. Note that the apparent weak fluxes in the MIZ are due to the reduction of the surface area and thus flux to maintain equal weighting between machine learning methods. The SAZ clearly dominates the annual uptake of CO_2 in the Southern Ocean, but the interannual variability is dominated by the PFZ. An interesting point of the SAZ is that the seasonal cycle of wind speed (strong in winter, weak in summer) opposes that of ΔpCO_2 sink (weak in winter, strong in summer). The net result is that, compared to ΔpCO_2, the seasonal amplitude of FCO_2 is reduced. The same effect shifts the mean flux in the PFZ, but does not affect the amplitude, where

outgassing is amplified in winter and the sink is weaker than if wind speed was constant. Lastly, Figures S3a,d show that the Indian sector of the Southern Ocean dominate both uptake (SAZ) and the interannual variability (PFZ).

S4 Uncertainty of the transition anomalies

The transition anomalies are not calculated from the mean of the three methods. Rather we calculate the anomalies for each individual method with:

$$a_{n(p')} = \overline{s_n}_{(p)} - \overline{s_n}_{(p-1)} \quad \text{(S2)}$$

where *s* are the estimates for a particular model, *n* represents an individual model and *p* represents P1 to P4. The result, $a_{n(p')}$ thus represents the anomaly for two periods for a particular model. We then calculate the average of the anomalies with:

$$a_{p'} = \frac{1}{N} \cdot \sum_{n=1}^{N} a_{n(p')} \quad \text{(S3)}$$

where *N* is 3, the number of models. We then calculate the standard deviation of the three anomalies ($e_{p'}$), which is analogous to the between-model error, with:

$$e_{p'} = \sqrt{\frac{1}{N} \cdot \sum_{n=1}^{N} (a_{n(p')} - \overline{a_{n(p')}})^2} \quad \text{(S4)}$$

where the terms are consistent with those above. We use $e_{p'}$ as an uncertainty threshold where anomalies are only considered significant if $|a_{p'}| > e_{p'}$. These regions are masked in Figures 5a-c and 6a-c. Figure S4 shows the winter (a-c) and summer (d-f) $e_{p'}$ for each transition anomaly.

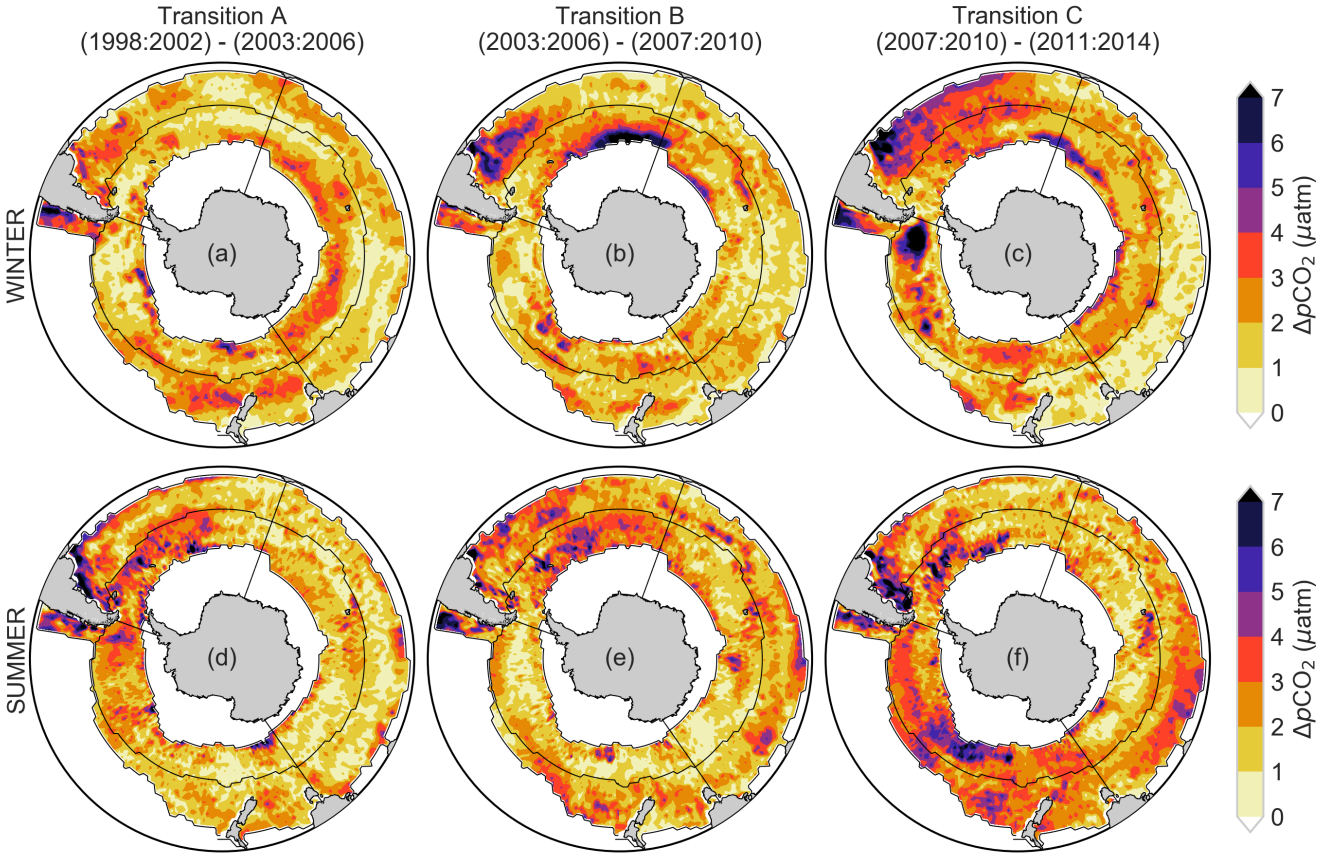

Figure S4: Maps of the standard deviation between empirical methods for the anomalies. These are used as thresholds for ΔpCO_2 in Figures 5(a-c) and 6(a-c) for winter and summer respectively. When the standard deviation exceeds the absolute value average anomaly, the values are masked as shown in Figures 5 and 6.

60

S5 Additional driver variables

Here we show additional variables that accompany Figures 5 and 6. Figure S5 shows winter Chl-*a*, u- and v-components of wind and Figure S6 shows summer MLD, u- and v-components of wind. These variables were not included in the main analyses as they did not contribute significant information to the proxy variables already present (wind stress, SST and MLD/Chl-*a*). It is interesting to note that the u- and v- components of wind speed highlight the zonally asymmetric dipole during winter (Figures S5d,e,g,h) and the annular dipole during summer (Figures S6d,e).

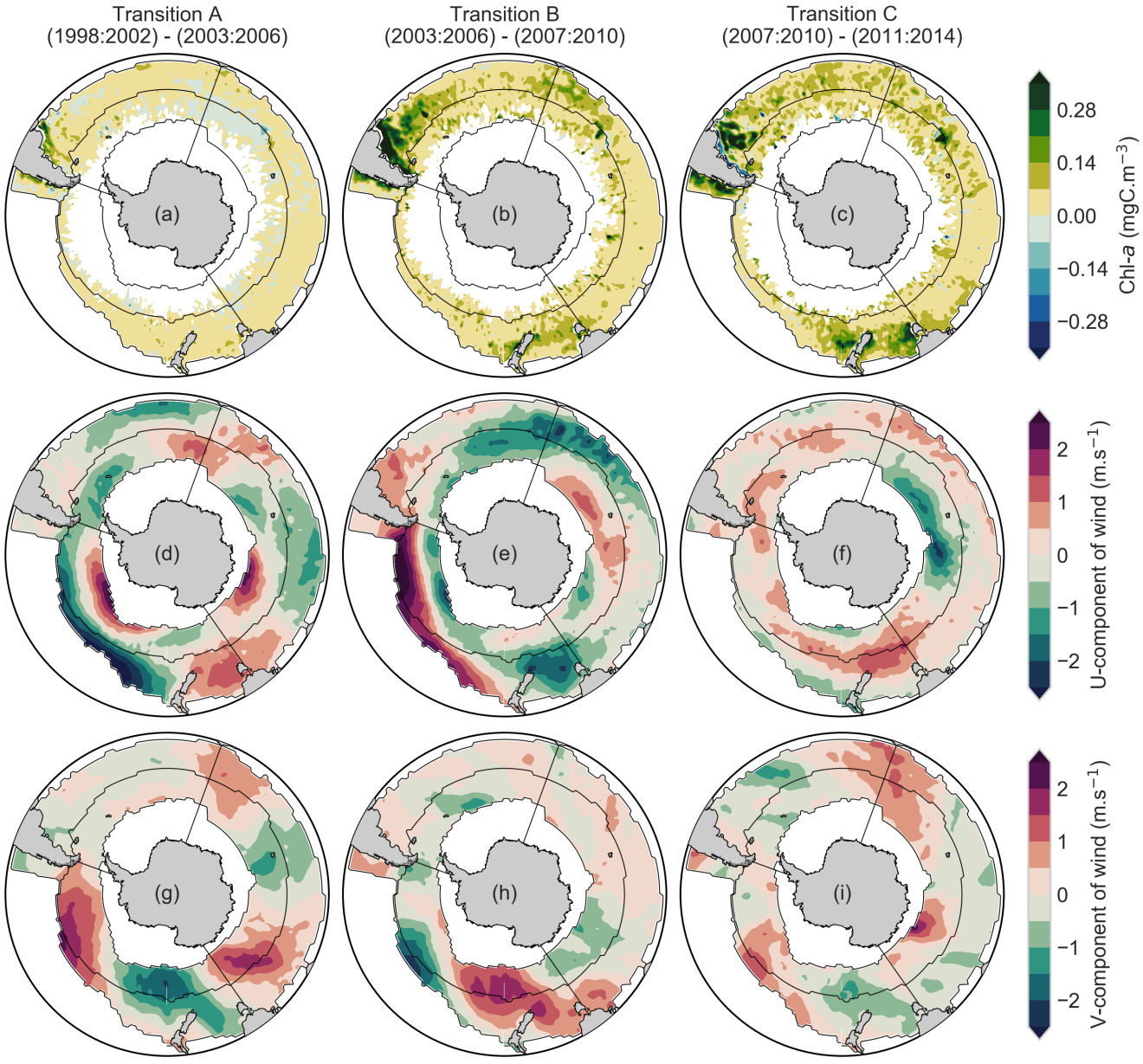

Figure S5: Relative anomalies of winter chlorophyll-a (a-c), u- (d-f), and v-components (g-i) of wind for four periods (as shown above each column). The thin black lines show the boundaries for each of the nine regions described by the biomes (Fay and McKinley, 2014a) and basin boundaries.

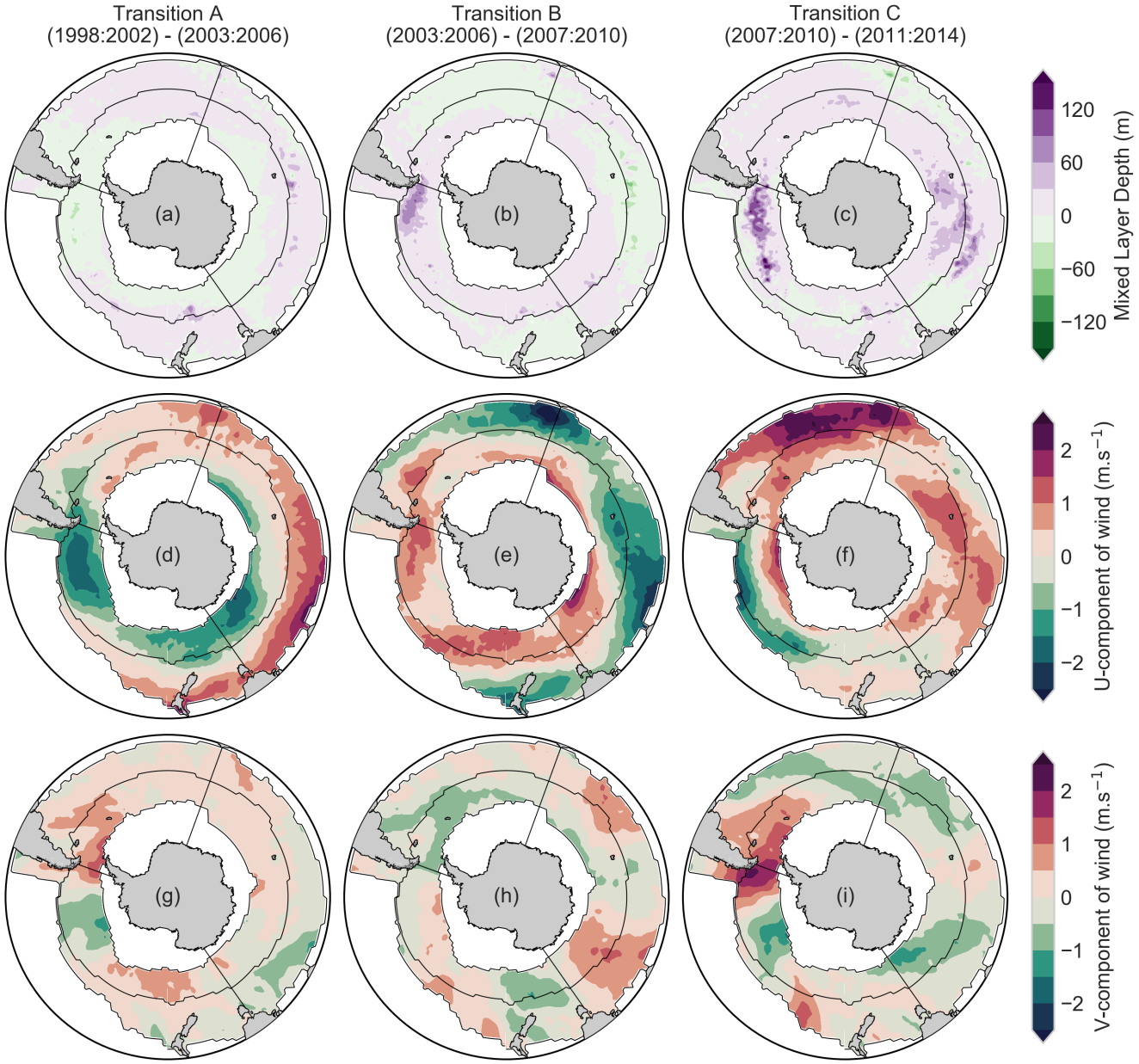

Figure S6: Relative anomalies of summer mixed layer depth (a-c), u- (d-f), and v-components (g-i) of wind for four periods (as shown above each column).. The thin black lines show the boundaries for each of the nine regions described by the biomes (Fay and McKinley, 2014a) and basin boundaries.

References

Abernathey, R., Marshall, J. C., & Ferreira, D. (2011). The Dependence of Southern Ocean Meridional Overturning on Wind Stress. *Journal of Physical Oceanography*, *41*(12), 2261–2278. https://doi.org/10.1175/JPO-D-11-023.1

Arrigo, K. R., van Dijken, G. L., & Bushinsky, S. (2008). Primary production in the Southern Ocean, 1997-2006. *Journal of Geophysical Research*, *113*(8), 1997–2006. https://doi.org/10.1029/2007JC004551

Atlas, R., Hoffman, R. N., Ardizzone, J., Leidner, S. M., Jusem, J. C., Smith, D. K., & Gombos, D. (2011). A Cross-calibrated, Multiplatform Ocean Surface Wind Velocity Product for Meteorological and Oceanographic Applications. *Bulletin of the American Meteorological Society*, *92*(2), 157–174. https://doi.org/10.1175/2010BAMS2946.1

Bakker, D. C. E., Hoppema, M., Schr, M., Geibert, W., & Baar, H. J. W. De. (2008). A rapid transition from ice covered CO2-rich waters to a biologically mediated CO2 sink in the eastern Weddell Gyre. *Biogeosciences*, *5*, 1373–1386.

Bakker, D. C. E., Pfeil, B., Landa, C. S., Metzl, N., O'Brien, K. M., Olsen, A., … Xu, S. (2016). A multi-decade record of high-quality fCO2 data in version 3 of the Surface Ocean CO2 Atlas (SOCAT). *Earth System Science Data*, *8*(2), 383–413. https://doi.org/10.5194/essd-8-383-2016

Barnes, E. A., & Hartmann, D. L. (2010). Dynamical Feedbacks of the Southern Annular Mode in Winter and Summer. *Journal of the Atmospheric Sciences*, *67*(2007), 2320–2330. https://doi.org/10.1175/2010JAS3385.1

Boyd, P. W., & Ellwood, M. J. (2010). The biogeochemical cycle of iron in the ocean. *Nature Geoscience*, *3*(10), 675–682. https://doi.org/10.1038/ngeo964

Butterworth, B. J., & Miller, S. D. (2016). Air-sea exchange of carbon dioxide in the Southern Ocean and Antarctic marginal ice zone. *Geophysical Research Letters*, *43*(13), 7223–7230. https://doi.org/10.1002/2016GL069581

Carranza, M. M., & Gille, S. T. (2015). Southern Ocean wind-driven entrainment enhances satellite chlorophyll-a through the summer. *Journal of Geophysical Research: Oceans*, *120*(1), 304–323. https://doi.org/10.1002/2014JC010203

CDIAC. (2017). *Multi-laboratory compilation of atmospheric carbon dioxide data for the period 1957-2016*. NOAA Earth System Research Laboratory, Global Monitoring Division. https://doi.org/10.15138/G3CW4Q

de Boyer Montégut, C., Madec, G., Fischer, A. S., Lazar, A., & Iudicone, D. (2004). Mixed layer depth over the global ocean: An examination of profile data and a profile-based climatology. *Journal of Geophysical Research*, *109*(12), 1–20. https://doi.org/10.1029/2004JC002378

DeVries, T., Holzer, M., & Primeau, F. (2017). Recent increase in oceanic carbon uptake driven by weaker upper-ocean overturning. *Nature*, *542*(7640), 215–218. https://doi.org/10.1038/nature21068

Dufour, C. O., Sommer, J. Le, Gehlen, M., Orr, J. C., Molines, J.-M., Simeon, J., & Barnier, B. (2013). Eddy compensation and controls of the enhanced sea-to-air CO2 flux during positive phases of the Southern Annular Mode. *Global Biogeochemical Cycles*, *27*(3), 950–961. https://doi.org/10.1002/gbc.20090

Fay, A. R., & McKinley, G. A. (2014). Global open-ocean biomes: Mean and temporal variability. *Earth System Science Data*, *6*(2), 273–284. https://doi.org/10.5194/essd-6-273-2014

Fay, A. R., McKinley, G. A., & Lovenduski, N. S. (2014). Southern Ocean carbon trends: Sensitivity to methods. *Geophysical Research Letters*, *41*(19), 6833–6840. https://doi.org/10.1002/2014GL061324

Fogt, R. L., Jones, J. M., & Renwick, J. (2012). Seasonal zonal asymmetries in the southern annular mode and their impact on regional temperature anomalies. *Journal of Climate*, *25*(18), 6253–6270. https://doi.org/10.1175/JCLI-D-11-00474.1

Gade, K. (2010). A Non-singular Horizontal Position Representation. *Journal of Navigation*, *63*(3), 395–417. https://doi.org/10.1017/S0373463309990415

Gregor, L., Kok, S., & Monteiro, P. M. S. (2017). Empirical methods for the estimation of Southern Ocean CO2: support vector and random forest regression. *Biogeosciences*, *14*(23), 5551–5569. https://doi.org/10.5194/bg-14-5551-2017

Gurney, K. R., Law, R. M., Denning, A. S., Rayner, P. J., Pak, B. C., Baker, D., … Taguchi, S. (2004). Transcom 3 inversion intercomparison: Model mean results for the estimation of seasonal carbon sources and sinks. *Global Biogeochemical Cycles*, *18*(1), n/a-n/a. https://doi.org/10.1029/2003GB002111

Hauck, J., Völker, C., Wang, T., Hoppema, M., Losch, M., & Wolf-Gladrow, D. A. (2013). Seasonally different carbon flux changes in the Southern Ocean in response to the southern annular mode. *Global Biogeochemical Cycles*, *27*(4), 1236–1245. https://doi.org/10.1002/2013GB004600

Hoppema, M., Fahrbach, E., Stoll, M. H. C., & de Baar, H. J. W. (1999). Annual uptake of atmospheric CO2 by the Weddell sea derived from a surface layer balance, including estimations of entrainment and new production. *Journal of Marine Systems*, *19*(4), 219–233. https://doi.org/10.1016/S0924-7963(98)00091-8

Ishii, M., Inoue, H. Y., Matsueda, H., & Tanoue, E. (1998). Close coupling between seasonal biological production and dynamics of dissolved inorganic carbon in the Indian Ocean sector and the western Pacific Ocean sector of the Antarctic Ocean. *Deep-Sea Research Part I: Oceanographic Research Papers*, *45*(7), 1187–1209. https://doi.org/10.1016/S0967-0637(98)00010-7

Jones, S. D., Le Quéré, C., & Rdenbeck, C. (2012). Autocorrelation characteristics of surface ocean pCO2 and air-sea CO2 fluxes. *Global Biogeochemical Cycles*, *26*(2), 1–12. https://doi.org/10.1029/2010GB004017

Kanamitsu, M., Ebisuzaki, W., Woollen, J., Yang, S. K., Hnilo, J. J., Fiorino, M., & Potter, G. L. (2002). NCEP-DOE AMIP-II reanalysis (R-2). *Bulletin of the American Meteorological Society*, *83*(11), 1631–1643+1559. https://doi.org/10.1175/BAMS-83-11-1631

Khatiwala, S., Tanhua, T., Mikaloff Fletcher, S. E., Gerber, M., Doney, S. C., Graven, H. D., … Sabine, C. L. (2013). Global ocean storage of anthropogenic carbon. *Biogeosciences*, *10*(4), 2169–2191. https://doi.org/10.5194/bg-10-2169-2013

Landschützer, P., Gruber, N., & Bakker, D. C. E. (2016). Decadal variations and trends of the global ocean carbon sink. *Global Biogeochemical Cycles*, *30*(10), 1396–1417. https://doi.org/10.1002/2015GB005359

Landschützer, P., Gruber, N., & Bakker, D. C. E. (2017). An updated observation-based global monthly gridded sea surface pCO2 and air-sea CO2 flux product from 1982 through 2015 and its monthly climatology (NCEI Accession 0160558) Version 2.2.

Landschützer, P., Gruber, N., Bakker, D. C. E., & Schuster, U. (2014). Recent variability of the global ocean carbon sink. *Global and Planetary Change*, 927–949. https://doi.org/10.1002/2014GB004853.Received

Landschützer, P., Gruber, N., Haumann, F. A., Rödenbeck, C., Bakker, D. C. E., Van Heuven, S. M. A. C., … Wanninkhof, R. H. (2015). The reinvigoration of the Southern Ocean carbon sink. *Science*, *349*(6253), 1221–1224. https://doi.org/10.1126/science.aab2620

Le Quéré, C., Rödenbeck, C., Buitenhuis, E. T., Conway, T. J., Langenfelds, R., Gomez, A., … Heimann, M. (2007). Saturation of the Southern Ocean CO2 Sink Due to Recent Climate Change. *Science*, *316*(5832), 1735–1738. https://doi.org/10.1126/science.1137004

Lenton, A., Codron, F., Bopp, L., Metzl, N., Cadule, P., Tagliabue, A., & Le Sommer, J. (2009). Stratospheric ozone depletion reduces ocean carbon uptake and enhances ocean acidification. *Geophysical Research Letters*, *36*(12), 1–5. https://doi.org/10.1029/2009GL038227

Lenton, A., & Matear, R. J. (2007). Role of the Southern Annular Mode (SAM) in Southern Ocean CO2 uptake. *Global Biogeochemical Cycles*, *21*(2), 1–17. https://doi.org/10.1029/2006GB002714

Lenton, A., Metzl, N., Takahashi, T. T., Kuchinke, M., Matear, R. J., Roy, T., … Tilbrook, B. (2012). The observed evolution of oceanic pCO2 and its drivers over the last two decades. *Global Biogeochemical Cycles*, *26*(2), 1–14. https://doi.org/10.1029/2011GB004095

Lenton, A., Tilbrook, B., Law, R. M., Bakker, D. C. E., Doney, S. C., Gruber, N., … Takahashi, T. T. (2013). Sea-air CO2 fluxes in the Southern Ocean for the period 1990-2009. *Biogeosciences*, *10*(6), 4037–4054. https://doi.org/10.5194/bg-10-4037-2013

Lévy, M., Iovino, D., Resplandy, L., Klein, P., Madec, G., Tréguier, A. M., … Takahashi, K. (2012). Large-scale impacts of submesoscale dynamics on phytoplankton: Local and remote effects. *Ocean Modelling*, *43–44*, 77–93. https://doi.org/10.1016/j.ocemod.2011.12.003

Lovenduski, N. S., Gruber, N., & Doney, S. C. (2008). Toward a mechanistic understanding of the decadal trends in the Southern Ocean carbon sink. *Global Biogeochemical Cycles*, *22*(3), 9. https://doi.org/10.1029/2007GB003139

Lovenduski, N. S., Gruber, N., Doney, S. C., & Lima, I. D. (2007). Enhanced CO2 outgassing in the Southern Ocean from a positive phase of the Southern Annular Mode. *Global Biogeochemical Cycles*, *21*(2), 1–14. https://doi.org/10.1029/2006GB002900

Mahadevan, A., D'Asaro, E., Lee, C., & Perry, M. J. (2012). Eddy-Driven Stratification Initiates North Atlantic Spring Phytoplankton Blooms. *Science*, *337*(6090), 54–58. https://doi.org/10.1126/science.1218740

Mahadevan, A., Tagliabue, A., Bopp, L., Lenton, A., Mémery, L., & Lévy, M. (2011). Impact of episodic vertical fluxes on sea surface pCO2. *Philosophical Transactions of the Royal Society*, *369*(1943), 2009–2025. https://doi.org/10.1098/rsta.2010.0340

Maritorena, S., & Siegel, D. A. (2005). Consistent merging of satellite ocean color data sets using a bio-optical model. *Remote Sensing of Environment*, *94*(4), 429–440. https://doi.org/10.1016/j.rse.2004.08.014

Marshall, G. J. (2003). Trends in the Southern Annular Mode from observations and reanalyses. *Journal of Climate*, *16*(24), 4134–4143. https://doi.org/10.1175/1520-0442(2003)016<4134:TITSAM>2.0.CO;2

McGillicuddy, D. J. (2016). *Mechanisms of Physical-Biological-Biogeochemical Interaction at the Oceanic Mesoscale*. *Annual Review of Marine Science* (Vol. 8). https://doi.org/10.1146/annurev-marine-010814-015606

McNeil, B. I., & Matear, R. J. (2013). The non-steady state oceanic CO2 signal: Its importance, magnitude and a novel way to detect it. *Biogeosciences*, *10*(4), 2219–2228. https://doi.org/10.5194/bg-10-2219-2013

Menemenlis, D., Campin, J., Heimbach, P., Hill, C. N., Lee, T., Nguyen, A., … J-M. Campin. (2008). ECCO2 : High Resolution Global Ocean and Sea Ice Data Synthesis. *Mercator Ocean Quarterly Newsletter*, *31*(October), 13–21. Retrieved from http://www.mercator-ocean.fr/content/download/691/5904/version/1/file/lettre_31_en.pdf#page=13

Meredith, M. P. (2016). Understanding the structure of changes in the Southern Ocean eddy field. *Geophysical Research Letters*, *43*(11), 5829–5832. https://doi.org/10.1002/2014JC010066.Received

Metzl, N., Brunet, C., Jabaud-Jan, A., Poisson, A., & Schauer, B. (2006). Summer and winter air-sea CO2 fluxes in the Southern Ocean. *Deep-Sea Research Part I: Oceanographic Research Papers*, *53*(9), 1548–1563. https://doi.org/10.1016/j.dsr.2006.07.006

Mongwe, N. P., Chang, N., & Monteiro, P. M. S. (2016). The seasonal cycle as a mode to diagnose biases in modelled CO 2 fluxes in the Southern Ocean. *Ocean Modelling*, *106*, 90–103. https://doi.org/10.1016/j.ocemod.2016.09.006

Monteiro, P. M. S., Gregor, L., Lévy, M., Maenner, S., Sabine, C. L., & Swart, S. (2015). Intraseasonal variability linked to sampling alias in air-sea CO2 fluxes in the Southern Ocean. *Geophysical Research Letters*, *42*(20), 8507–8514. https://doi.org/10.1002/2015GL066009

Munro, D. R., Lovenduski, N. S., Takahashi, T. T., Stephens, B. B., Newberger, T., & Sweeney, C. (2015). Recent evidence for a strengthening CO2 sink in the Southern Ocean from carbonate system measurements in the Drake Passage (2002-2015). *Geophysical Research Letters*, *42*(18), 7623–7630. https://doi.org/10.1002/2015GL065194

Nicholson, S. A., Lévy, M., Llort, J., Swart, S., & Monteiro, P. M. S. (2016). Investigation into the impact of storms on sustaining summer primary productivity in the Sub-Antarctic Ocean. *Geophysical Research Letters*, *43*(17), 9192–9199. https://doi.org/10.1002/2016GL069973

Pfeil, B., Olsen, A., Bakker, D. C. E., Hankin, S., Koyuk, H., Kozyr, A., … Yoshikawa-Inoue, H. (2013). A uniform, quality controlled Surface Ocean CO2 Atlas (SOCAT). *Earth System Science Data*, *5*(1), 125–143. https://doi.org/10.5194/essd-5-125-2013

Reynolds, R. W., Smith, T. M., Liu, C., Chelton, D. B., Casey, K. S., & Schlax, M. G. (2007). Daily high-resolution-blended analyses for sea surface temperature. *Journal of Climate*, *20*(22), 5473–5496. https://doi.org/10.1175/2007JCLI1824.1

Rödenbeck, C., Bakker, D. C. E., Gruber, N., Iida, Y., Jacobson, A. R., Jones, S. D., … Zeng, J. (2015). Data-based estimates of the ocean carbon sink variability - First results of the Surface Ocean pCO2 Mapping intercomparison (SOCOM). *Biogeosciences*, *12*(23), 7251–7278. https://doi.org/10.5194/bg-12-7251-2015

Rödenbeck, C., Keeling, R. F., Bakker, D. C. E., Metzl, N., Olsen, A., Sabine, C. L., & Heimann, M. (2013). Global surface-ocean pCO2 and sea-Air CO2 flux variability from an observation-driven ocean mixed-layer scheme. *Ocean Science*, *9*(2), 193–216. https://doi.org/10.5194/os-9-193-2013

Rodgers, K. B., Aumont, O., Mikaloff Fletcher, S. E., Plancherel, Y., Bopp, L., de Boyer Montégut, C., … Wanninkhof, R. H. (2014). Strong sensitivity of Southern Ocean carbon uptake and nutrient cycling to wind stirring. *Biogeosciences*, *11*(15), 4077–4098. https://doi.org/10.5194/bg-11-4077-2014

Sabine, C. L., Hankin, S., Koyuk, H., Bakker, D. C. E., Pfeil, B., Olsen, A., … Yoshikawa-Inoue, H. (2013). Surface Ocean CO2 Atlas (SOCAT) gridded data products. *Earth System Science Data*, *5*(1), 145–153. https://doi.org/10.5194/essd-5-145-2013

Sasse, T. P., McNeil, B. I., & Abramowitz, G. (2013). A novel method for diagnosing seasonal to inter-annual surface ocean carbon dynamics from bottle data using neural networks. *Biogeosciences*, *10*(6), 4319–4340. https://doi.org/10.5194/bg-10-4319-2013

Shetye, S. S., Mohan, R., Patil, S., Jena, B., Chacko, R., George, J. V., … Sudhakar, M. (2015). Oceanic pCO2 in the Indian sector of the Southern Ocean during the austral summer–winter transition phase. *Deep Sea Research Part II: Topical Studies in Oceanography*, *118*, 250–260. https://doi.org/10.1016/j.dsr2.2015.05.017

Swart, N. C., & Fyfe, J. C. (2012). Observed and simulated changes in the Southern Hemisphere surface westerly wind-stress. *Geophysical Research Letters*, *39*(16), 6–11. https://doi.org/10.1029/2012GL052810

Swart, N. C., Fyfe, J. C., Gillett, N., & Marshall, G. J. (2015). Comparing trends in the southern annular mode and surface westerly jet. *Journal of Climate*, *28*(22), 8840–8859. https://doi.org/10.1175/JCLI-D-15-0334.1

Swart, S., Speich, S., Ansorge, I. J., & Lutjeharms, J. R. E. (2010). An altimetry-based gravest empirical mode south of Africa: 1. Development and validation. *Journal of Geophysical Research*, *115*(C3), 1–19. https://doi.org/10.1029/2009JC005299

Swart, S., Thomalla, S. J., & Monteiro, P. M. S. (2015). The seasonal cycle of mixed layer dynamics and phytoplankton biomass in the Sub-Antarctic Zone: A high-resolution glider experiment. *Journal of Marine Systems*, *147*, 103–115. https://doi.org/10.1016/j.jmarsys.2014.06.002

Tagliabue, A., Bowie, A. R., Philip, W., Buck, K. N., Johnson, K. S., & Saito, M. A. (2017). The integral role of iron in ocean biogeochemistry. *Nature*, *543*(7643), In Press. https://doi.org/10.1038/nature21058

Tagliabue, A., Sallée, J.-B., Bowie, A. R., Lévy, M., Swart, S., & Boyd, P. W. (2014). Surface-water iron supplies in the Southern Ocean sustained by deep winter mixing. *Nature Geoscience*, *7*(March), 314–320. https://doi.org/10.1038/NGEO2101

Takahashi, T. T., Olafsson, J., Goddard, J. G., Chipman, D. W., & Sutherland, S. C. (1993). Seasonal variation of CO 2 and nutrients in the high-latitude surface oceans: A comparative study. *Global Biogeochemical Cycles*, *7*(4), 843–878. https://doi.org/10.1029/93GB02263

Takahashi, T. T., Sutherland, S. C., Sweeney, C., Poisson, A., Metzl, N., Tilbrook, B., … Nojiri, Y. (2002). Global sea-air CO2 flux based on climatological surface ocean pCO2, and seasonal biological and temperature effects. *Deep-Sea Research Part II: Topical Studies in Oceanography*, *49*(9–10), 1601–1622. https://doi.org/10.1016/S0967-0645(02)00003-6

Takahashi, T. T., Sutherland, S. C., Wanninkhof, R. H., Sweeney, C., Feely, R. A., Chipman, D. W., … de Baar, H. J. W. (2009). Climatological mean and decadal change in surface ocean pCO2, and net sea–air CO2 flux over the global oceans. *Deep-Sea Research Part II: Topical Studies in Oceanography*, *56*(8–10), 554–577. https://doi.org/10.1016/j.dsr2.2008.12.009

Thomalla, S. J., Fauchereau, N., Swart, S., & Monteiro, P. M. S. (2011). Regional scale characteristics of the seasonal cycle of chlorophyll in the Southern Ocean. *Biogeosciences*, *8*(10), 2849–2866. https://doi.org/10.5194/bg-8-2849-2011

Wang, S., & Moore, J. K. (2012). Variability of primary production and air-sea CO2 flux in the Southern Ocean. *Global Biogeochemical Cycles*, *26*(1), 1–12. https://doi.org/10.1029/2010GB003981

Wanninkhof, R. H., Asher, W. E., Ho, D. T., Sweeney, C., & McGillis, W. R. (2009). Advances in Quantifying Air-Sea Gas Exchange and Environmental Forcing*. *Annual Review of Marine Science*, *1*(1), 213–244. https://doi.org/10.1146/annurev.marine.010908.163742

Weiss, R. (1974). Carbon dioxide in water and seawater: the solubility of a non-ideal gas. *Marine Chemistry*, *2*(3), 203–215. https://doi.org/10.1016/0304-4203(74)90015-2

Wentz, F. J., Scott, J., Hoffman, R., Leidner, M., Atlas, R., & Ardizzone, J. (2015). Remote Sensing Systems Cross-Calibrated Multi-Platform (CCMP) 6-hourly ocean vector wind analysis product on 0.25 deg grid, Version 2.0. Retrieved March 5, 2017, from www.remss.com/measurements/ccmp

Whitt, D. B., Lévy, M., & Taylor, J. R. (2017). Low-frequency and high-frequency oscillatory winds synergistically enhance nutrient entrainment and phytoplankton at fronts. *Journal of Geophysical Research*, *122*(2), 1016–1041. https://doi.org/10.1002/2016JC012400